MICROSTRUCTURE-SENSITIVE FATIGUE MODELING OF MEDICAL-GRADE FINE WIRE

A Thesis
Presented to
The Academic Faculty

by

Brian Charles Clark

In Partial Fulfillment
of the Requirements for the Degree
Master of Science in the
George W. Woodruff School of Mechanical Engineering

Georgia Institute of Technology
December 2016

MICROSTRUCTURE-SENSITIVE FATIGUE MODELING OF MEDICAL-GRADE FINE WIRE

Approved by:

Dr. Richard W. Neu, Advisor
George W. Woodruff School of Mechanical Engineering
School of Materials Science and Engineering
Georgia Institute of Technology

Dr. David L. McDowell
George W. Woodruff School of Mechanical Engineering
School of Materials Science and Engineering
Georgia Institute of Technology

D.I. Dr. Markus Reiterer
Sr. Principle Scientist
Corporate Core Technologies
Medtronic, PLC.

Date Approved: November 03, 2016

ACKNOWLEDGEMENTS

This work would not have come to fruition were it not for the assistance and support I received from a great many people. I would like to express my thanks to my advisor, Dr. Richard Neu for providing direction throughout the research process, and for his expertise and helpful advice. I would also like to thank the members of my committee, Dr. David McDowell and Dr. Markus Reiterer for their feedback and input to the development of the model. The financial sponsorship of Dr. Reiterer of Medtronic, PLC through a grant to the Center for Computational Materials Design is gratefully acknowledged. Furthermore, the calibration data provided by Jim Hallquist of Medtronic, PLC was critical to the success of the model. I would also like to thank a number of my colleagues at Georgia Tech for their helpful insights and suggestions. I am particularly indebted to Dr. Gustavo Castelluccio, whose frequent consultations were a great aid to my development as a researcher and to the thoroughness of the research. I would also like to thank Dr. William Musinski for conversations on modeling techniques and my lab-mates Kyle Brindley and Ashley Nelson for providing a sounding board for new ideas. Lastly, I would like to express my gratitude to my parents, for nurturing my interest in the sciences and to my wife, Audrey for her love, patience and encouragement throughout my studies.

TABLE OF CONTENTS

ACKNOWLEDGEMENTS . . . . . **iii**

LIST OF TABLES . . . . . **vi**

LIST OF FIGURES . . . . . **vii**

SUMMARY . . . . . **x**

I INTRODUCTION **1**

1.1 Motivation 1

1.2 Research Objective 2

1.3 Thesis Layout 3

II BACKGROUND **4**

2.1 MP35N Material Specifications 4

2.1.1 Characterization of Microstructure Attributes 5

2.2 Rotating Beam Bending Fatigue 8

2.3 Schaffer Fatigue Results 11

2.4 Microstructure-sensitive Fatigue Modeling 12

2.5 Fatigue Life Considerations 14

III MODELING METHODOLOGY **16**

3.1 Microstructure Generation and SVEs 16

3.2 Constitutive Model 17

3.2.1 Inelastic Constitutive Equations 17

3.3 Fatigue Indicator Parameters 19

3.3.1 Fatemi-Socie Parameter 20

3.3.2 Selection of Averaging Volumes 21

3.4 Extreme Value Statistics 24

3.5 Correlation to Life 25

IV COMPUTATIONAL IMPLEMENTATION 26
4.1 Microstructure Generation and Meshing 28
4.1.1 User Input Parameters 28
4.1.2 Instantiation of Statistical Volume Elements 34
4.1.3 Mesh Quality Study 38
4.2 Constitutive Model Parameter Fitting 46
4.2.1 Calibration Experiments 46
4.2.2 Initial Parameter Calibration 49
4.2.3 Intermediate Parameter Calibration 51
4.2.4 Revised Parameter Calibration 52
V RESULTS AND DISCUSSION 55
5.1 FIP-Life Correlations 55
5.1.1 Effect of Inclusion Proximity to Surface 55
5.1.2 Identifying the Crack Incubation to Microcrack Growth Transition 64
VI CONCLUSIONS 73
VII RECOMMENDATIONS FOR FURTHER STUDY 75
7.1 Ranking of Microstructure Attributes by Fatigue Potency 75
7.1.1 NMI Morphology 75
7.1.2 NMI-matrix Interface 76
7.1.3 Alternative Crack Initiation Sites 76
REFERENCES 78

LIST OF TABLES

2.1 Nominal chemical compositions of MP35N & 35N-LT given as wt %. From [2]. 5

3.1 Summary of main constitutive equations implemented by the UMAT 19

3.2 Volumes (in μm^3) of the FIP AVs for a 4 μm cubic NMI. 24

4.1 Independent (user defined) input parameters for microstructure generation 29

4.2 Summary of size and run-time measures for the eight mesh density levels 41

4.3 Variables, parameters and coefficients used in constitutive relations . 45

4.4 Values of the constitutive parameters for the initial model calibration (UMAT v28) 49

4.5 Results of DFT atomistic calculations for Ni-35Co-20Cr-10Mo alloy calculated at 0 Kelvin (ShunLi Shang, personal communication, 14 August 2013). 50

4.6 Values of the constitutive parameters for the intermediate model calibration (UMAT v110) 51

4.7 Values of the constitutive parameters for the revised model calibration (UMAT v110e) 53

5.1 Values of NMI geometry parameters at each level of the virtual DoE . 57

5.2 Relationships between beam-bending stress reported at the wire apex (S_a) and stress (S_{YY}) and strain (ε_a) amplitudes applied to the SVE . 59

5.3 Fitting Parameters for GEV CDFs 63

5.4 Fitting Parameters for Gumbel CDFs 64

LIST OF FIGURES

2.1 Inclusions in MP35N fine wire. (a) Sharp cuboidal TiN inclusion, partially debonded from the matrix. (b) Globular Al_2O_3 (alumina) inclusion near the wire surface. Note differences in scale. From [19] 5

2.2 FIB cross-section micrograph illustrating the fine grain structure and deformation twins. From [14]. 6

2.3 Grain size distributions of four wire cross-sections Af-1 through Af-4. From [7]. 7

2.4 EBSD accompanied by pole figures of low-Ti MP35N showing strong $\langle 111 \rangle$ texture. From [14]. 8

2.5 Configuration of wire fixed in a RBBF test system showing relevant parameters for fatigue loading. Taken from [2]. 9

2.6 Illustration of the variation of normal stress across a wire cross-section 10

2.7 Schematic illustrating the dependence of S_{yy} stress amplitude on the location of a material point within the wire. Point A experiences twice the maximum stress of point B. 10

2.8 CDFs of fatigue lives of MP35N and 35N-LT under RBBF at 827 MPa stress amplitude. From [20] 11

2.9 Effect of inclusion depth (filled circles) and size (open circles) on fatigue life of MP35N wire at a stress amplitude of 620 MPa. From [20]. . . . 12

3.1 Schematic showing the positioning and naming conventions of selected FS AVs with respect to a 50% debonded cuboidal inclusion. 22

3.2 Measurement conventions for the FIP AVs with respect to a 50% debonded cuboidal NMI. 23

4.1 Block diagram of information flow through the component parts of the model, showing the software tools used for each step. 27

4.2 Stress-fields around a cuboidal NMI with various interface debonding scenarios. (2) Top-only debond. (3) Upper-half debond (4) All but bottom debond. The NMI has been removed for clarity. 31

4.3 Volume fraction breakdown of texture components for four different MP35N wire samples with four texture components each. From [7]. . 33

4.4 Cut-section view of an exemplary microstructure instantiation with 1000 grains. Grains are delineated by color. The cuboidal TiN NMI particle is shown in grey in the center. The width of the NMI is 4 μm and the SVE is 20 μm on each side. 35

4.5 2D illustration of ellipsoid grain placement showing coordinate systems and naming conventions used. For clarity, only a few elements are shown, and the inclusion is excluded. 37

4.6 PDF of a representative microstructure instantiation with 1000 grains comparing the achieved grain size distribution to the target distribution. 38

4.7 Targeted grain semi-axes ratios of a representative microstructure instantiation with 1000 grains. 39

4.8 Cut-section view of SVE generated for mesh quality study showing 64 cubic grains and central NMI. 40

4.9 Run-time (in seconds) for increasing number of elements along NMI edge. 42

4.10 Volume-averaged Full-Face FS response for increasing number of elements along NMI edge. 43

4.11 Volume-averaged Mid-Face FS response for increasing number of elements along NMI edge. 44

4.12 Strain-rate jump test on low-Ti MP35N as-drawn wire with strain rate alternating every 0.5% increment of strain. From [14]. 47

4.13 Strain Ratcheting Experiments showing the accumulation of strain over 300 cycles for ${S_{max}}^1 = 1400$ MPa and ${S_{max}}^2 = 1500$ MPa. 48

4.14 Plot of $\log(N)$ vs peak strain (mm/mm) for the LCF1 experiment. The rate of strain accumulation stabilizes after 10 cycles. 48

4.15 Comparisons of the initial and intermediate parameter calibrations to the rate jump uniaxial tension test. Experimental data from [14]. . . 52

4.16 Comparisons of the initial and intermediate parameter calibrations to the LCF1 strain ratcheting experiment. 53

4.17 Sensitivity of the effective elastic modulus to SVE texture. 54

5.1 Subset of an SVE showing definitions of TiN particle geometry as related to the wire surface. 56

5.2 Loading profile applied to each SVE to simulate RBBF. Points A and B are the step endpoints used in the FS FIP calculations. 57

5.3 Selection of stress amplitude for an SVE. Stress amplitude S_{YY} decreases linearly with NMI depth x_c due to the stress gradient generated in bending. Note that the x axis for depth is opposite the global X axis. 60

5.4 Extreme-value FS parameter values for four distinct NMI depths and corresponding stress amplitudes 61

5.5 Life correlations of the model fit to experimental data. The modified T-M fit is performed at the 0.75 μm level resulting in a correlation coefficient α of 1.129×10^{-5} μm-cycles. 62

5.6 CDFs of the Fatigue-life correlations with corresponding GEV distributions. 63

5.7 CDFs of the fatigue-life correlations with fitted Gumbel distributions. 64

5.8 Prasad et al. S-N data for as-drawn low-Ti MP35N wire [14]. 66

5.9 Comparison of Extreme-Value FS parameter responses using weighting coefficients $k^* = 1$ and $k^* = 0.2$. 68

5.10 Fatigue-life correlation to Prasad et al. RBBF data at 620 MPa with T-M correlation coefficient $\alpha = 4.995 \times 10^{-7}$ μm-cycles. 69

5.11 Close-in view of the point of divergence between the T-M correlation to the RBBF data at 680 MPa and 1×10^5 cycles. 70

5.12 Weighted variability (Ω_{FS}) in EV FS response parameters at the five stress amplitudes modeled with 10 microstructure instantiations each. 72

SUMMARY

This work presents a model to assess the microstructure-sensitive high-cycle fatigue (HCF) performance of thin MP35N alloy wires used as conductors in cardiac leads. The major components of this model consist of a microstructure generator that creates a mesh of a statistically representative microstructure, a finite element analysis using a crystal plasticity constitutive model to determine the local response behavior of the microstructure, and a postscript employing fatigue indicating parameters (FIPs) to assess the fatigue crack incubation potency at fatigue hotspots.

The crystal structure of the MP35N alloy, which contains major elements (wt %) 35Ni-35Co-20Cr-10Mo, is modeled as single-phase, face-centered cubic (fcc) material, and the calibration of the constitutive behavior is based on monotonic tensile and cyclic ratcheting stress-strain response data generated on the wire. A non-random texture generation scheme is introduced to approximate the strong fiber texture developed by wire drawing. Non-metallic inclusions (NMIs) have been shown to be detrimental in fatigue of MP35N wires by serving as fatigue crack nucleation sites. The model developed here considers the detrimental effects of NMIs using a stochastic framework. By evaluating multiple statistical volume elements (SVEs), the inherent statistical variability of inclusion-grain and grain-grain interactions at the NMI-matrix interface can be assessed. The fatigue crack incubation potency for selected microstructure attributes, boundary and interface conditions, and loading profiles is determined by computing the Fatemi-Socie (FS) multi-axial FIP over an appropriate volume of scale.

The extreme-value FS distributions were successfully correlated to rotating beam bending fatigue (RBBF) life data collected for MP35N fine wire. The correlation

indicates that the fatigue potency in RBBF is strongly influenced by the NMI proximity to the wire surface with the most severe case occurring when the NMI intersects the surface. A significant drop in fatigue potency is observed when the NMI is fully embedded in the wire. Fatigue-life correlations to a second set of RBBF data were performed in order to identify a transition life value between crack incubation and microcrack growth fatigue mechanisms. The transition life was identified as 1×10^5 cycles. The model has applications in numerous additional aspects of microstructure-sensitive HCF which can be explored in a future work.

CHAPTER I

INTRODUCTION

1.1 Motivation

A robust understanding of component fatigue behavior is critical for the medical device industry especially for permanently implantable, life sustaining applications where minimizing invasive procedures and treatments is highly desirable. In the case of cardiac pacing leads, the in-situ loading conditions are variable and difficult to quantify. Heart contractions create a low-amplitude, high-frequency load, and torso and arm movements add higher amplitude, but low frequency loading. In the high cycle fatigue regime, the fatigue life of fine wires is dominated by crack incubation. Once formed, a fatigue crack grows quickly to reach the instability point due to the geometric constraints of the wire, after which ductile (fast) fracture occurs. Fatigue crack nucleation in fine wires is a stochastic process controlled by defects within the microstructure. These defects occur in the drawn wire as surface scratches or non-metallic inclusions (NMIs). Understanding the role these defects play in fatigue life variability is critical to the design of fatigue resistant lead wires.

Past studies [20] have employed statistical Monte Carlo initiation life models to predict such variability. However, these models are constrained by a limited capability to represent the microstructure of the lead wires. Through the use of a crystal plasticity finite element model (CPFEM) governed by a set of constitutive laws, many different microstructural attributes can be modeled and quickly assessed for their impact on fatigue. Analysis of process-structure-properties relationships using computational tools is a key aspect of the Materials Genome Initiative (MGI) [12]. MGI

calls on governmental agencies, academic institutions and industrial partners to cooperate in accelerating the pace of materials development. The goal is to reduce by half the typical material design lifecycle. The MGI infrastructure consists of three parts: experimental tools, computational tools and data science tools. Once developed, these tools can be adapted rapidly to collect and analyze material performance for different materials, applications and processing routes. The current project contributes to the computational tools aspect of materials development by creating software tools to predict the high-cycle fatigue (HCF) performance of the MP35N alloy in the fine wire configuration. Knowledge of the salient microstructure attributes also contributes to the fundamental materials science understanding of this alloy.

1.2 Research Objective

The work presented in this thesis aims to link microstructure attributes of MP35N fine wire with its HCF performance under application-relevant loading conditions through the application of structure-property relations. At the present time, no known CPFEM models have been developed for MP35N fine wire or for MP35N in the bulk form. Although Schaffer [19] developed a numerical model for fine wire MP35N incorporating the influence of a number of microstructural inputs via Monte Carlo methods, his model does not account for polycrystalline plasticity which is known to play a significant role in HCF. The objective of this research is to develop a computational CPFEM model for MP35N fine wire capable of elucidating differences in fatigue performance due to variability of microstructure attributes. This includes:

1. Formulation of constitutive relations that capture the rate sensitivity and kinematic hardening behavior of MP35N fine wire

2. Calibration of these constitutive relations to experimental data

3. Development of a microstructure generation and meshing protocol to recreate

salient MP35N microstructure attributes in a stochastic, finite-element framework

4. Selection of appropriate response parameters to assess fatigue performance

5. Characterization of the extreme-value distributions of the selected response parameters

6. Validation of the newly-developed CPFEM model against experimental data

1.3 Thesis Layout

Chapter 2 provides background on the MP35N alloy system and the microstructure of MP35N fine wires and reviews previous fatigue models and fatigue testing techniques. Chapter 3 describes the modeling methodology employed in this research, including the generation of virtual microstructures, constitutive model framework, selection of fatigue indicating parameters and life correlation methods. Chapter 4 details the computational implementation of the model into software codes and considers the calibration of the constitutive model behavior using selected experiments. Chapter 5 presents the results of two studies using the newly developed model: (1) the effect of NMI-surface proximity and (2) the identification of crack incubation to microcrack growth transition life value. The implications of each study are also discussed. Chapter 6 summarizes the main conclusions from the research. Finally, Chapter 7 proposes some recommendations for further study to extend the development and applications of the model in relation to the current effort.

CHAPTER II

BACKGROUND

2.1 MP35N Material Specifications

MP35N (ASTM F562) is a quaternary, low temperature superalloy. It has a nominal composition of 35% nickel, 35% cobalt, 20% chromium and 10% molybdenum. The full composition by weight percent as specified by ASTM [2] is given in Table 2.1. The high amount of nickel produces a metastable fcc crystal structure. MP35N in the bulk form was first developed by SPS technologies for use in NASA cryogenic fastener applications. The fine wire form of MP35N has found use in surgical implants due its excellent corrosion resistance and biocompatibility [13] as well as its high strength and fatigue resistance. Applications include catheters, stylets and pacing leads.

Production of wires is accomplished by drawing a rod through successively smaller dies with intermediate annealing steps. The drawing process produces significant anisotropy in the material with strong texture components in the {001}, {111} and {113} [7,14,23]. Drawing also contributes to a fine grain structure. Grain size for fine wire is typically 1-5 μm, compared with 35 μm or greater for the bulk material. Figure 2.2 is a FIB micrograph of a transverse section of the wire, revealing the fine grain structure. In the bulk material, HCP platelets form through the Suzuki mechanism [1, 5]. The HCP phase has not been observed in fine wire specimens [14, 23] or bulk specimens under room-temperature deformation [17], leading to its characterization as a single-phase material. Plastic deformation is accommodated through both slip and intra-granular twinning [23]. Twins are found to be between 1-10 nm in thickness. Once formed, deformation twins also act as a hardening mechanism, impeding the motion of dislocations.

The presence of non-metallic inclusions (NMIs) is a primary driver of fatigue in MP35N wires [20]. Two types of inclusion particles have been identified: cuboidal titanium nitride (TiN) and globular aluminum oxide (Al_2O_3). The former are typically larger in size (4-10 μm) compared to the later (1-5 μm). Example of these can be seen in Figure 2.1. A variant of the alloy designated 35N-LT was developed by Fort Wayne Metals. Titanium content was reduced below 0.01% to eliminate TiN particles, improving fatigue performance. In this work, the terms full-Ti or low-Ti will be used to differentiate between the MP35N or 35N-LT variants when necessary.

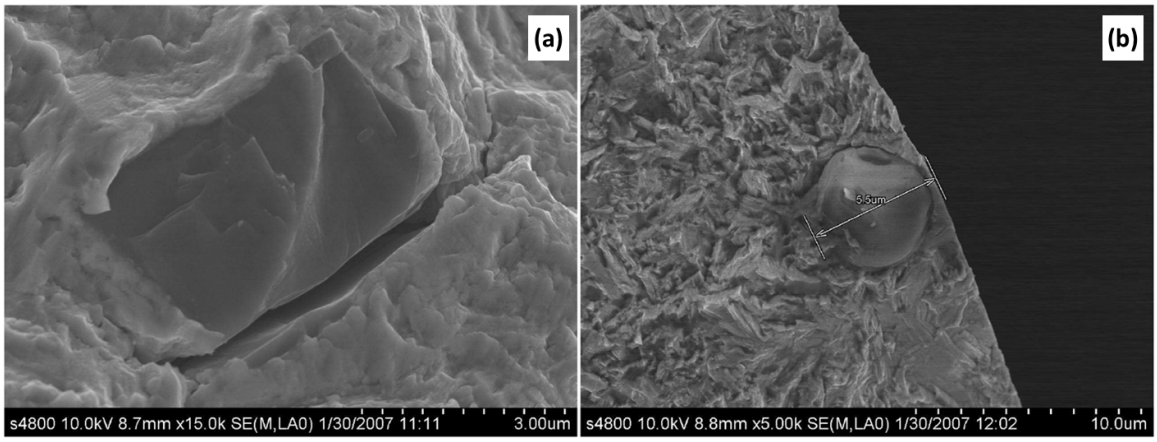

Figure 2.1: Inclusions in MP35N fine wire. (a) Sharp cuboidal TiN inclusion, partially debonded from the matrix. (b) Globular Al_2O_3 (alumina) inclusion near the wire surface. Note differences in scale. From [19]

Table 2.1: Nominal chemical compositions of MP35N & 35N-LT given as wt %. From [2].

Alloy	C	Mn	Si	P	S	Cr	Ni	Mo	Fe	Ti	B	Co
MP35N	0.025	0.15	0.15	0.015	0.010	19.0-21.0	33.0-37.0	9.0-10.5	1.0	1.0	0.015	Bal.
35N-LT	0.010	0.06	0.03	0.002	0.001	20.58	34.82	9.51	0.52	≤ 0.01	0.010	Bal.

2.1.1 Characterization of Microstructure Attributes

The salient microstructure attributes of the MP35N fine wire were experimentally characterized in order to provide realistic input for virtual microstructure instantiation. Grain size, and texture distributions were produced via EBSD imaging of a

transverse wire cross-section. Grain morphology was estimated by comparing longitudinal and transverse EBSD cross-sections but was not formally measured.

2.1.1.1 Grain Size Distribution

Experimental characterization of MP35N fine wire by Focused Ion Beam (FIB) micrographs (Figure 2.2) has shown the grain size to be on the order of 1-5 μm. Variation in grain size is usually considered to follow a lognormal distribution. This can be seen from Figure 2.3 which shows the frequency of grain sizes as area fractions generated from four MP35N cross-sections, denoted Af-1 through Af-4. The largest distribution with the peak at 2.05 μm (Af-4) was selected to emulate in this work, since it is more representative of Fig 2.2.

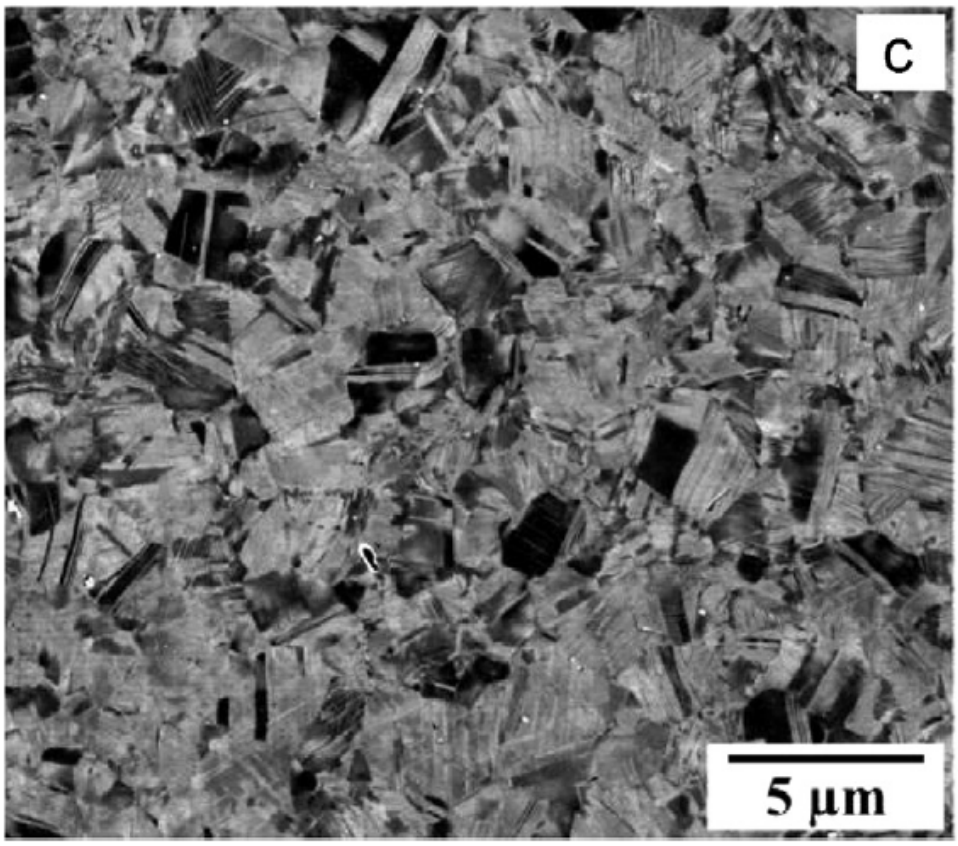

Figure 2.2: FIB cross-section micrograph illustrating the fine grain structure and deformation twins. From [14].

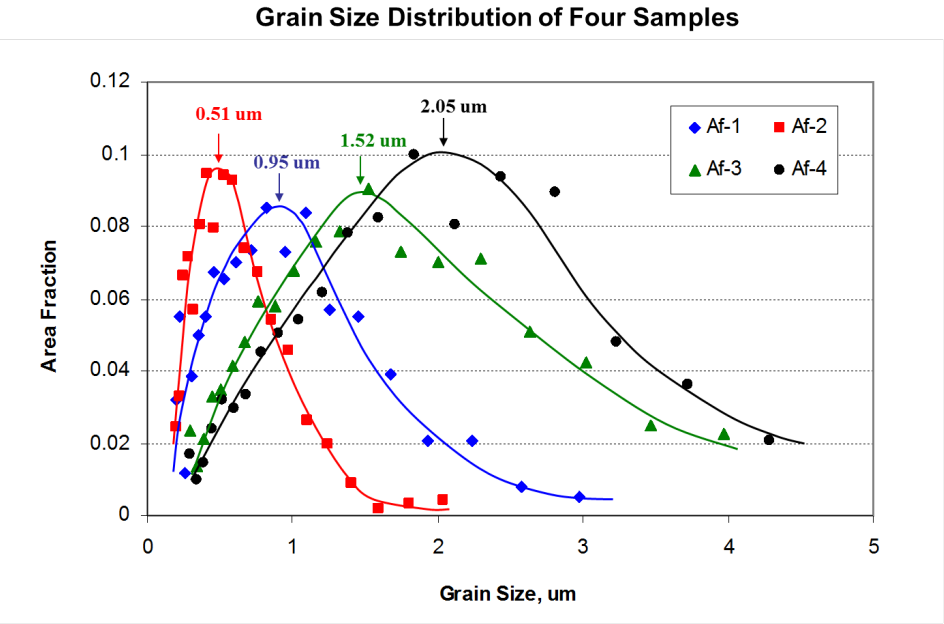

Figure 2.3: Grain size distributions of four wire cross-sections Af-1 through Af-4. From [7].

2.1.1.2 Texture

MP35N in its cold-drawn condition exhibits a strong fiber texture produced as a result of the wire drawing. The texture is shown in Figure 2.4. The texture map on the left and pole figures on the right illustrate the concentrations around the $\langle 111 \rangle$ and $\langle 100 \rangle$ orientations.

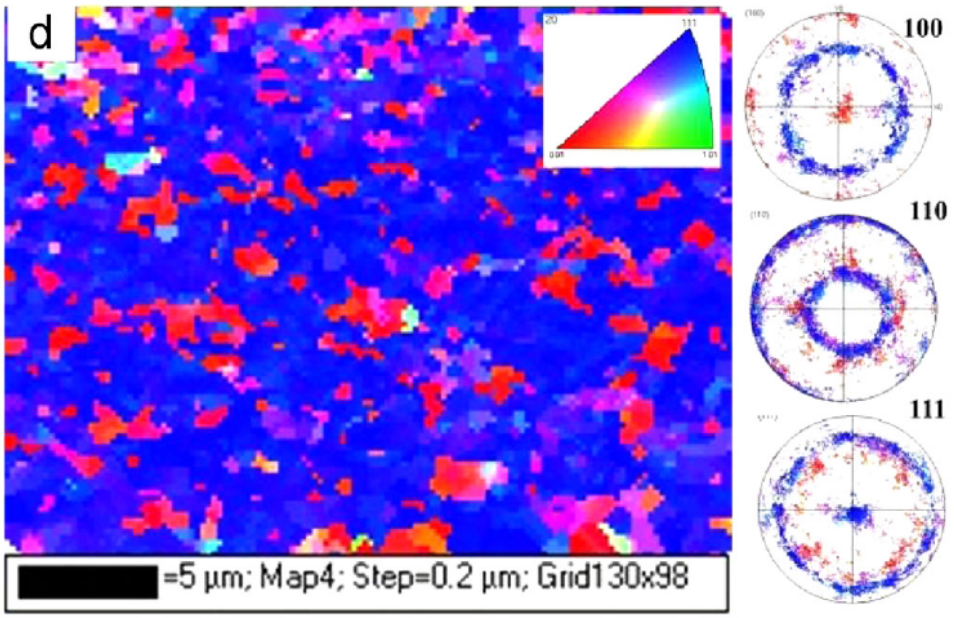

Figure 2.4: EBSD accompanied by pole figures of low-Ti MP35N showing strong ⟨111⟩ texture. From [14].

2.2 Rotating Beam Bending Fatigue

One type of fatigue experiment commonly conducted for fine wires is known as Rotating Beam Bending Fatigue (RBBF). RBBF is an ASTM standardized test method (E2948-14). A schematic of the wire configuration in the test system is shown in Figure 2.5.

A length of wire is bent into a 180 degree arc and fixed at both ends by a rotary chuck and bushing. Applying a rotational moment to the chuck results in a fully reversed ($R = -1$) bending load as the wire rotates about its neutral axis. The stresses and strains generated by RBBF can be determined from beam bending theory, assuming purely elastic deformation and a homogeneous, isotropic material response. The bending stress amplitude scales with the local wire curvature which is highest at the wire apex, and approaches zero at either end. The magnitude of bending strain at the apex is related to the minimum bend radius ρ_{min} by the relation

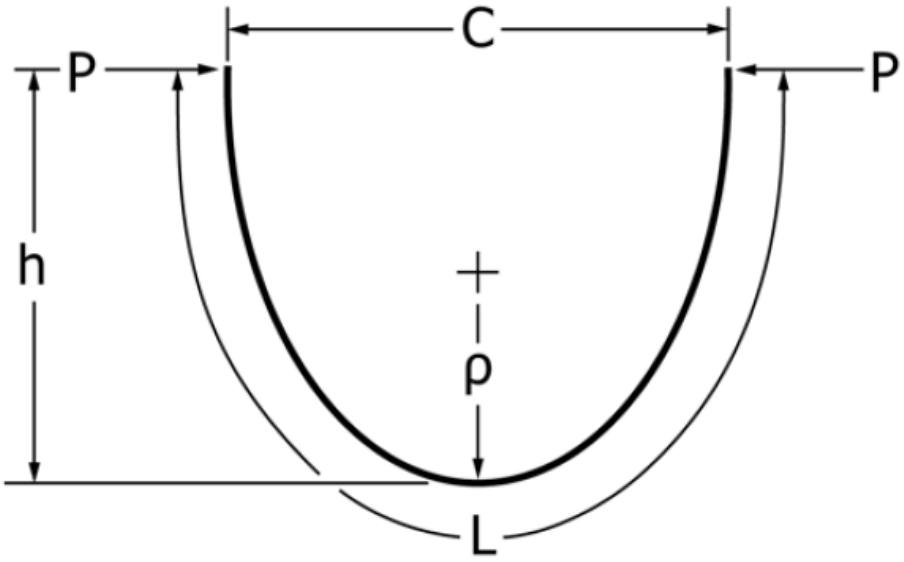

Figure 2.5: Configuration of wire fixed in a RBBF test system showing relevant parameters for fatigue loading. Taken from [2].

$$\varepsilon_a = \frac{d/2}{\rho_{min}} \tag{2.1}$$

where d is the wire diameter. The minimum bend radius is controlled by the center distance C according to

$$\rho_{min} = 0.417C \tag{2.2}$$

and

$$C = 1.198\,\frac{E\,d}{S_a} \tag{2.3}$$

where E is the elastic modulus of the wire, and S_a is the fully-reversed stress amplitude. The wire length L and loop height h are related to C by constant factors. The bending produces a non-uniform stress profile across the wire cross-section, driven by the bending moment about the neutral axis as shown in Figure 2.6.

The outer fiber of the wire is loaded in tension while the inner fiber undergoes compression. The maximum tensile and compressive stresses have equal magnitude but opposite sign. As the wire rotates about its neutral axis each material point in

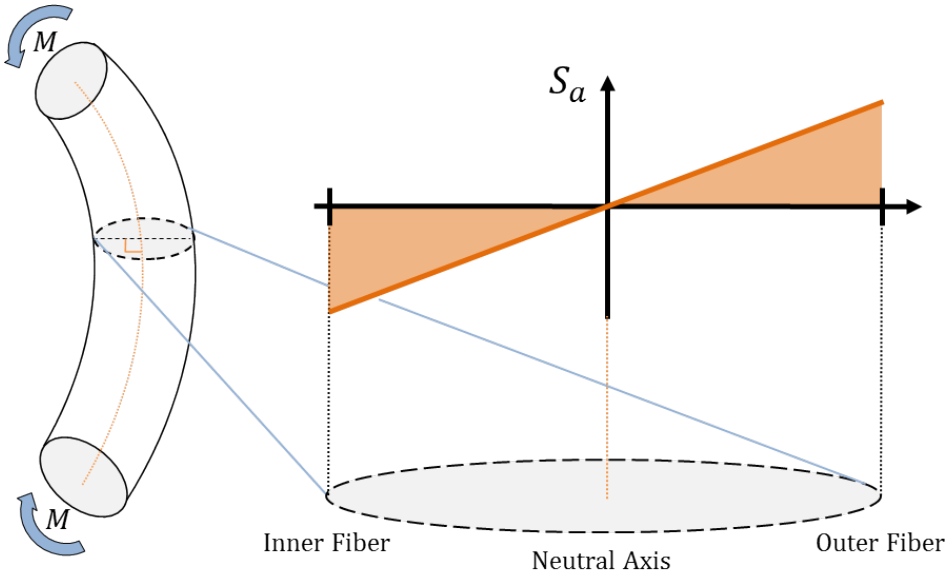

Figure 2.6: Illustration of the variation of normal stress across a wire cross-section

the wire experiences load reversal between tension and compression. The effective S_{yy} load amplitude depends on the distance away from the neutral axis. As shown in Figure 2.7, material point A on the surface of the wire experiences twice the S_{yy} stress amplitude of point B, which is located halfway between the surface and the neutral axis.

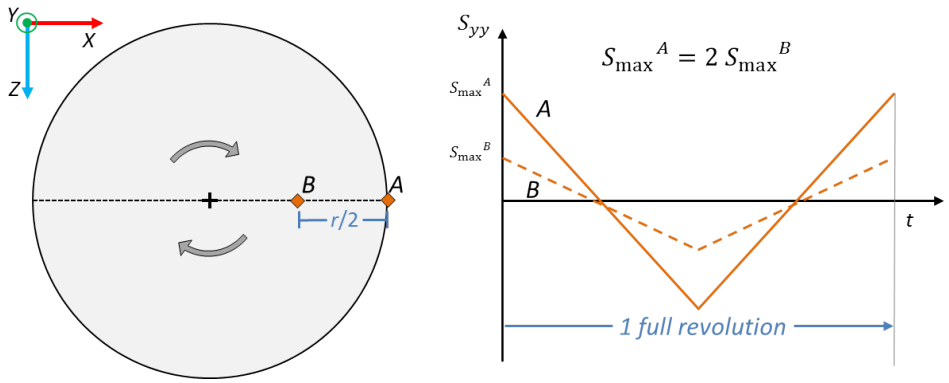

Figure 2.7: Schematic illustrating the dependence of S_{yy} stress amplitude on the location of a material point within the wire. Point A experiences twice the maximum stress of point B.

Because of the stress gradient across the wire cross-section, the effective S_{yy} load

amplitude at the site of crack initiation depends strongly on the distance of the site from the neutral axis. In the absence of complicating microstructural factors, the far-field loading conditions favor crack formation at the free surface. However, it is conceivable for a fatigue crack to initiate away from the surface if microstructural attributes located there combine to provide a significant driving force.

2.3 Schaffer Fatigue Results

An in-depth study of RBBF fatigue of the MP35N alloy system was conducted by Schaffer [19] in both the LCF and HCF regimes. Both the low and full Ti alloy variants were investigated. It was shown that the low-Ti alloy variant, 35N-LT performed better in RBBF than its counterpart, as seen in the cumulative distribution function (CDF) of Figure 2.8. Moreover, the 35N-LT data revealed a bimodal life distribution, with one group of failures occurring in the range between 2.2×10^5 and 2×10^6 cycles, while a separate group of failures occurred in a higher range at greater than 1×10^7 cycles.

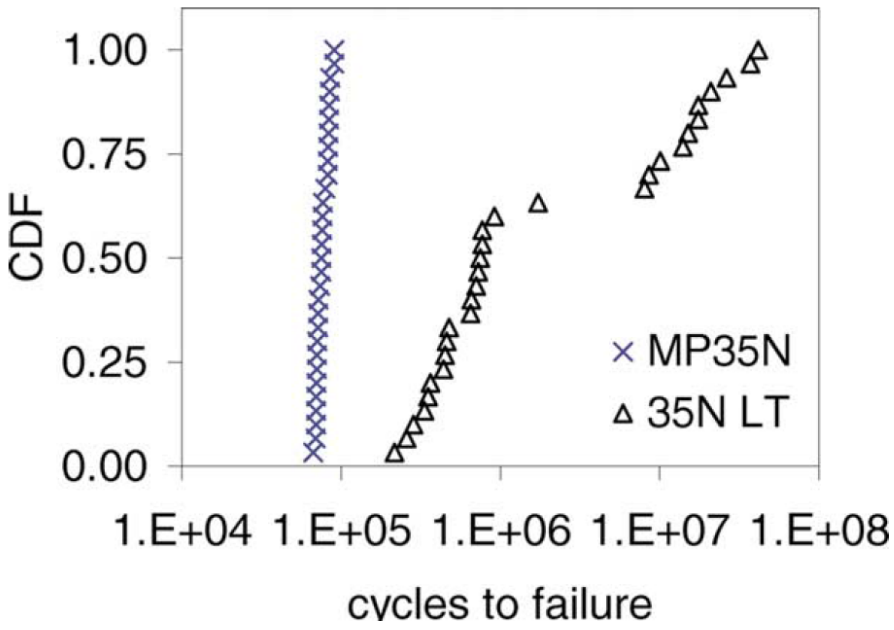

Figure 2.8: CDFs of fatigue lives of MP35N and 35N-LT under RBBF at 827 MPa stress amplitude. From [20]

The separation between the two groups was attributed to differences in the crack initiation site: in the lower range group cracks predominantly formed by small (1-5 μm) alumina inclusions at or very near the surface, while in the higher cycle group cracks initiated at subsurface particles greater than 0.5 μm below the surface. The dependence of fatigue life on inclusion particle depth from the surface is also present in the full-Ti version of the alloy albeit at lower stress amplitudes. This trend is illustrated in Figure 2.9. Here filled circles denote the inclusion depth from the wire surface and open circles represent the size of each inclusion, such that each fatigue experiment performed is displayed by two points – one filled and one open – on the plot.

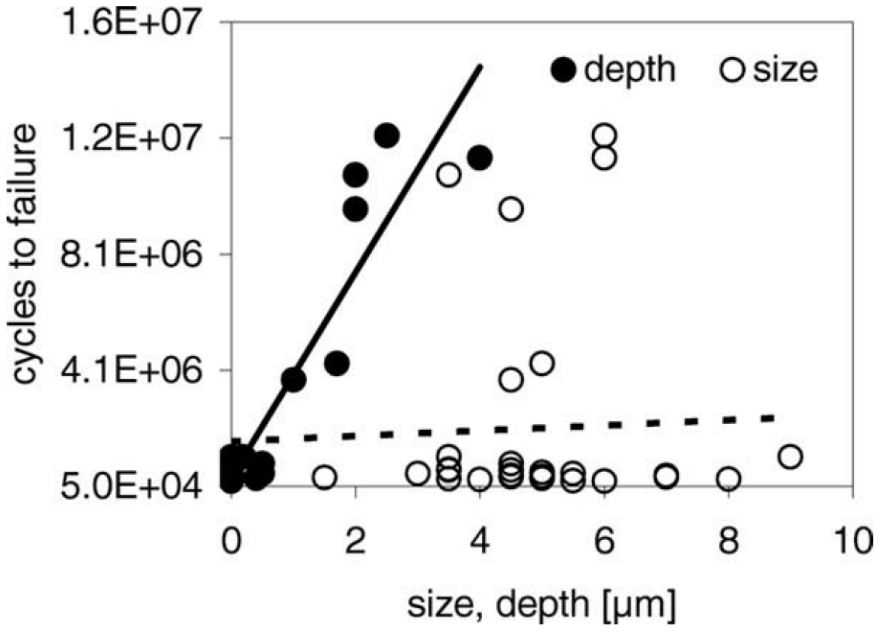

Figure 2.9: Effect of inclusion depth (filled circles) and size (open circles) on fatigue life of MP35N wire at a stress amplitude of 620 MPa. From [20].

2.4 Microstructure-sensitive Fatigue Modeling

Microstructure-sensitive fatigue models are attempts to represent scatter in fatigue life by explicitly considering the effects of microstructure. The microstructure attributes

considered may include grain size and texture, phases, precipitates, non-metallic inclusions, voids or other pre-existing flaws at the scale of the microstructure.

The major components of a microstructure-sensitive fatigue model involve:

1. A representation of one or more microstructural attributes which vary in conformance to some prescribed distributions

2. A method for applying representative fatigue loading and tracking the evolution of local stresses and strains

3. A metric to evaluate fatigue damage potency. This involves combining key response parameters in a manner that provide an indication of the fatigue damage potency of the applied loading in light of the microstructure attributes represented. Response parameters include stress-based, strain-based, energy-based or critical-plane based response parameters.

Historically, empirical methods of have been used to provide an estimation of fatigue life. The most well-known of these approaches are the Basquin equation for HCF and the Coffin-Manson equation for LCF [24]. The combination of these two equations via Hookes law provides a fatigue equation which spans high and low cycle fatigue. Various modifications have been proposed to adapt this model to non-zero mean stress, notch effects, etc. These empirical methods rely on extensive fatigue experiments to fit their coefficients and convey no information about the microstructure. Microstructure-sensitive fatigue models implemented with modern computational tools can better represent known physical phenomena that lead to fatigue including slip localization and plastic strain heterogeneity due to geometrical features (notches etc) and grain-grain and grain-inclusion interactions.

Some of the specific applications of microstructure-sensitive fatigue models are as follows:

1. Link experimentally observed scatter in fatigue life data to known damage mechanisms

2. Provide an estimate of minimum fatigue life for a given alloy, processing, and cyclic loading history

3. Establish rankings of microstructure attributes most detrimental to life.

These applications have been considered in recent work. Musinski [11] implemented a crystal plasticity finite element model to examine microstructurally small fatigue crack growth in both smooth and notched Ni-base superalloy specimens incorporating the effect of debonded inclusion particles and grain boundary effects. Przybyla [16] used extreme-value marked correlation functions to identify and rank the influence of coupled microstructure attributes (grain orientation, misorientation and size) on fatigue damage in a Ni-base superalloy and two Ti alloys. Salajeghah [18] used weighted probability functions to investigate the surface to bulk transition in HCF crack initiations in both IN100 and C61 martensitic gear steel.

2.5 Fatigue Life Considerations

Life to failure of a metallic component is traditionally divided into initiation life and propagation life according to the equation

$$N_f = N_{inc} + N_p \tag{2.4}$$

Here, N_{inc} is the number of cycles required to incubate a crack, N_p is the number of cycles for the crack to propagate to failure. Propagation life can be further subdivided three crack growth regimes as

$$N_p = N_{msc} + N_{psc} + N_{lc} \tag{2.5}$$

where N_{msc} is the number of cycles from formation to a microstructurally small crack, N_{psc} is the number of cycles to grow to a physically small crack, and N_{lc} defines the long crack growth regime, which typically begins when the crack reaches the visual inspection limit through the onset of fast fracture. The boundaries of the crack growth regimes are not well defined. For the purposes of this model, we neglect the contribution of propagation life to the total life in MP35N wire fatigue based on the following reasoning:

1. Once incubated, cracks propagate to reach the instability point in relatively few cycles due to the small cross-sections of the fine wires.

2. The change in N_p with decreasing stress amplitude is minimal.

3. Under HCF and VHCF conditions the total cycles to failure is large, and the great majority of these contribute to crack incubation.

A simple example can illustrate this reasoning. Suppose the propagation life for any stress amplitude is the same, $N_p = 10,000$ cycles. Now consider two HCF RBBF specimens, one failing at $N_f = 100,000$ cycles, and another at $N_f = 1,000,000$ cycles. For the first specimen, 10% of all cycles are propagation, and for the second specimen only 1% of the total life is propagation. Based on this consideration, it is judged that the contribution to the fatigue life from crack propagation in the HCF regime will be less than 10% and can be neglected for the purposes of this model.

CHAPTER III

MODELING METHODOLOGY

3.1 Microstructure Generation and SVEs

In order to model the stochastic nature of metallic microstructures in a computationally feasible way, it is useful to employ Statistical Volume Elements (SVEs). These idealized volumes are constructed such that each identically-sized volume is a sample of the underlying distributions of the microstructure attributes. Each SVE contains a unique, random arrangement of grains and crystallographic textures which are sampled from experimentally characterized grain size and texture distributions.

The size of the volume must meet certain criteria to qualify as an SVE. The volume must be of the same length scale as the response parameters of interest, i.e. grain-scale plasticity. Additionally, the volume must be small enough such that the distribution of the local response parameters of interest within each SVE comprises a subset of all possible values. The SVE volume should be large enough relative to the grain size that the average stress-strain responses of multiple SVEs converges to the macroscopic stress-strain response determined by experiment.

The use of SVEs for numerical fatigue modeling offers advantages in computational efficiency. A limited number of SVEs (< 100) at each loading condition can adequately characterize the distribution of the desired response parameter. Variation of microstructure attributes between successive SVEs results in differences in the local stress-strain response. These differences can be quantified using Fatigue Indicating Parameters (FIPs) which serve as a proxy measure for fatigue crack formation.

3.2 Constitutive Model

The constitutive model for fine wire MP35N is adapted from a previous model by Shenoy [21] for Inconel 100, a Ni-based superalloy. The constitutive model describes the elastic and inelastic deformation through a set of equations derived from crystal plasticity and continuum mechanics. The shear strain rate $\dot{\gamma}$ depends on shear stress τ, and the evolution of two internal state variables (ISVs) – dislocation density ρ and backstress χ. In the fine wire configuration, MP35N consists of a single-phase FCC structure with intra-granular deformation twins. Slip is permitted only on the 12 octahedral systems $\langle 110 \rangle$ $\{111\}$. Deformation twins are not explicitly modeled, but are accounted for phenomenologically through two input parameters: twin volume fraction f_{tw} and twin spacing, t. Homogenization over deformation twins is necessary due to the limited spatial resolution of finite element modeling. The model seeks to predict damage processes at the scale of microns, while deformation twins have been shown by TEM imaging to have thicknesses of 1-10 nanometers [14, 23].

3.2.1 Inelastic Constitutive Equations

The inelastic shear strain rate on slip system α is given by a single-term flow rule

$$\dot{\gamma}^{(\alpha)} = \dot{\gamma_o} \left\langle \frac{|\tau^{(\alpha)} - \chi^{(\alpha)}| - \kappa^{(\alpha)}}{D^{(\alpha)}} \right\rangle^n sgn(\tau^{(\alpha)} - \chi^{(\alpha)}) \tag{3.1}$$

where $\dot{\gamma}_o$ is a shear strain rate constant, D is the drag stress, n is the flow exponent and κ is the threshold hardening parameter. D and n are fitting parameters that describe the resistance to plastic flow and the strain rate sensitivity, respectively. The second term used by Shenoy to account for thermally activated flow is removed for this isothermal model. Inelastic shear strain is zero until an isotropic threshold stress κ is attained. The threshold hardening equation depends on dislocation density ρ through a Taylor relation

$$\kappa^{(\alpha)} = \kappa_o^{(\alpha)} + \alpha_t \mu b \sqrt{\rho^{(\alpha)}} \tag{3.2}$$

where b is the burgers vector of MP35N, μ is the (resolved) shear modulus, α_t is a constant and κ_o is the initial critical resolved shear stress (CRSS) given by

$$\kappa_o^{(\alpha)} = [(\tau_o^{(\alpha)})^{n_k} + c_{gr}(d_{gr})^{-0.5} + c_{gr}(f_{tw})]^{\frac{1}{n_k}} \tag{3.3}$$

which depends on the lattice resistance, τ_o, the nominal grain size, d_{gr}, and the twin volume fraction f_{tw} as well as constants c_{gr} and n_k. Dislocation density ρ evolves by the equation

$$\dot{\rho}^{(\alpha)} = \sum_{\beta=1}^{12} h^{(\alpha\beta)} \left(\frac{k_1}{b\Lambda^{(\beta)}} - k_2 \rho^{(\beta)} \right) |\dot{\gamma}^{(\beta)}| \tag{3.4}$$

Here k_1 and k_2 are constants, $h^{(\alpha\beta)}$ is the hardening coefficient matrix, and Λ is the mean free path (MFP) for dislocation motion. The dislocation density affects both isotropic and kinematic hardening, as seen in Eqs. 3.2 and 3.7. At high dislocation densities typical of strongly cold-worked components, competition between dislocation formation and annihilation results in saturation of ρ due to the dynamic equilibrium between the first and second terms of Eq. 3.4. The hardening coefficient matrix takes the form

$$h^{(\alpha\beta)} = h_o \delta^{(\alpha\beta)} \tag{3.5}$$

where h_o is a constant and δ is the Kronecker delta. Here $\alpha = \beta$ represents self-hardening slip systems and $\alpha \neq \beta$ represents latent slip or cross-hardening. Due to the low stacking-fault energy (SFE) of MP35N, cross-slip is assumed to be negligible. The MFP Λ is a measure of the obstacle-free movement distance available to a dislocation on a given slip system. In MP35N, it is described by the harmonic mean of three distances: the grain size d_{gr}, twin spacing t and the spacing of immobile dislocations which scales inversely with the square root of dislocation density.

$$\frac{1}{\Lambda^{(\beta)}} = \frac{1}{d_{gr}} + \frac{1}{t} + k_3 \sqrt{\rho^{(\beta)}} \tag{3.6}$$

The backstress evolves according to

$$\dot{\chi}^{(\alpha)} = C_\chi [\eta \mu b \sqrt{\rho^{(\alpha)}} sgn(\tau^{(\alpha)} - \chi^{(\alpha)}) - \chi^{(\alpha)}] |\dot{\gamma}^{(\alpha)}| \tag{3.7}$$

where C_χ is a fitting parameter and η depends on d_{gr}, t and Λ by the relation

$$\eta = \eta_o \Lambda^{(\alpha)} \left(\frac{1}{d_{gr}} + \frac{1}{t} \right) \tag{3.8}$$

The backstress equation contains two terms: an accumulation term that depends on the dislocation density on the current slip system, and a dynamaic recovery term dependent on the current value of χ representing the influence of dislocation annihilation. The backstress ISV captures the Bauschinger effect and plastic ratcheting that occurs under cyclic loading as a result of non-uniform dislocation pile-up at grain and twin boundaries. The constitutive equations implemented by the model are summarized in Table 3.1.

Table 3.1: Summary of main constitutive equations implemented by the UMAT

Flow Rule	$\dot{\gamma}^{(\alpha)} = \dot{\gamma}_o \left\langle \frac{\lvert \tau^{(\alpha)} - \chi^{(\alpha)} \rvert - \kappa^{(\alpha)}}{D^{(\alpha)}} \right\rangle^n sgn(\tau^{(\alpha)} - \chi^{(\alpha)})$
Threshold Hardening	$\kappa^{(\alpha)} = \kappa_o^{(\alpha)} + \alpha_t \mu b \sqrt{\rho^{(\alpha)}}$
Initial CRSS	$\kappa_o^{(\alpha)} = [(\tau_o^{(\alpha)})^{n_k} + c_{gr}(d_{gr})^{-0.5} + c_{gr}(f_{tw})]^{\frac{1}{n_k}}$
Backstress Evolution	$\dot{\chi}^{(\alpha)} = C_\chi [\eta \mu b \sqrt{\rho^{(\alpha)}} sgn(\tau^{(\alpha)} - \chi^{(\alpha)}) - \chi^{(\alpha)}] \lvert \dot{\gamma}^{(\alpha)} \rvert$
Eta	$\eta = \eta_o \Lambda^{(\alpha)} \left(\frac{1}{d_{gr}} + \frac{1}{t} \right)$
Dislocation Density Evolution	$\dot{\rho}^{(\alpha)} = \sum_{\beta=1}^{12} h^{(\alpha\beta)} \left(\frac{k_1}{b\Lambda^{(\beta)}} - k_2 \rho^{(\beta)} \right) \lvert \dot{\gamma}^{(\beta)} \rvert$
Hardening Coefficients	$h^{(\alpha\beta)} = h_o \delta^{(\alpha\beta)}$
Mean Free Path	$\frac{1}{\Lambda^{(\beta)}} = \frac{1}{d_{gr}} + \frac{1}{t} + k_3 \sqrt{\rho^{(\beta)}}$

3.3 Fatigue Indicator Parameters

Fatigue Indicator Parameters (FIPs) provide a way to determine the location and relative potency of fatigue hot-spots within a component after the application of

fatigue loading. FIPs are physically-based metrics that combine tensor quantities such as stresses or plastic strains occurring over a representative load cycle into a single scalar value which can be used to judge the relative fatigue potency. Numerous FIPs have been proposed and utilized for different materials and crack formation mechanisms.

3.3.1 Fatemi-Socie Parameter

The Fatemi-Socie (FS) parameter [6] was selected for use with the model for its ability to predict fatigue response in materials where crack formation is driven by localized cyclic shear strain. The parameter is based on the observation that cyclic fatigue cracks tend to form on planes aligned with the direction of maximum shear strain amplitude, but that magnitude of shear strain amplitude alone does not explain the lower rates of cracking in torsional fatigue compared to uniaxial. To account for this, the maximum plastic shear strain amplitude over a cycle is modified by the normal stress to the plane of maximum plastic shear strain. The FS parameter is given by

$$P_{FS} = \frac{\Delta\gamma^p_{max}}{2}\left[1 + k^* \frac{\sigma_n^{max}}{\sigma_Y}\right] \tag{3.9}$$

where $\Delta\gamma^p_{max}$ is the maximum range of plastic shear strain on the critical plane over a cycle and σ_n^{max} is the maximum stress normal to the critical plane. The maximum normal stress is normalized by the yield stress σ_Y and weighted by the coefficient k^*. The weighting coefficient can be estimated by correlating uniaxial to torsional fatigue data. Lacking torsional data for MP35N fine wire, k^* has been arbitrarily set to 1, which is within the range of values found in fatigue literature [3, 11]. The FS parameter as formulated in Eq. 3.9 is termed a critical plane type FIP since it accounts for preferential crack nucleation on cyclic shear planes. Musinski [9] considered two distinct critical plane types, crystallographic or non-crystallographic. The crystallographic formulation finds the critical plane by searching all available slip systems, while the non-crystallographic formulation takes the plane of maximum

cyclic shear strain in 3D space. The non-crystallographic formulation is used in this work to simplify computation. The choice of critical plane calculation methodology is not expected to significantly impact the parameter scaling.

3.3.2 Selection of Averaging Volumes

The FS parameter must be evaluated over an appropriate volume in order to provide a meaningful indication of fatigue crack formation potency. Two important considerations for averaging volume (AV) selection are size and sampling location within the SVE.

3.3.2.1 Size Considerations

Volume size is dictated by (a) the finite size of fatigue crack incubation, (b) regularization to eliminate mesh-size dependency and (c) desired level of smoothing over microstructural features such as grains. The term incubation is not well-defined in literature, having no single agreed-upon criteria. For the purposes of this research, a fatigue crack is considered incubated when the cracked area within the matrix approaches 1 μm^2. Therefore, the size of the volumes used will be of this same scale.

3.3.2.2 Sampling Location Considerations

Sampling location is associated with the locations of stress risers within the microstructure which provide the driving force for crack initiation. In many cases, the locations of stress risers are unknown a-priori so the entire SVE must be interrogated to locate them. However, when a hard NMI is present within the SVE, stress concentrations will occur along the inclusion-matrix interface, permitting a targeted application of sampling locations there. Salajegheh [18] found that inclusions which are half debonded from the matrix in an orientation perpendicular to the loading axis will generate their maximum stresses along the debonding perimeter. Under HCF conditions, stresses quickly approach their far-field values moving radially outward

away from the NMI surface, resulting in insufficient driving force to generate plasticity more than a few microns from the NMI interface. Because of this, AVs are sampled immediately adjacent to the NMI. Salajegheh showed that this sampling location corresponded to the locations of largest FIP magnitude for the 50% debonded NMI configuration [18]. Figure 3.1 illustrates the locations of selected FIP averaging volumes for the case of a 50% debonded TiN inclusion.

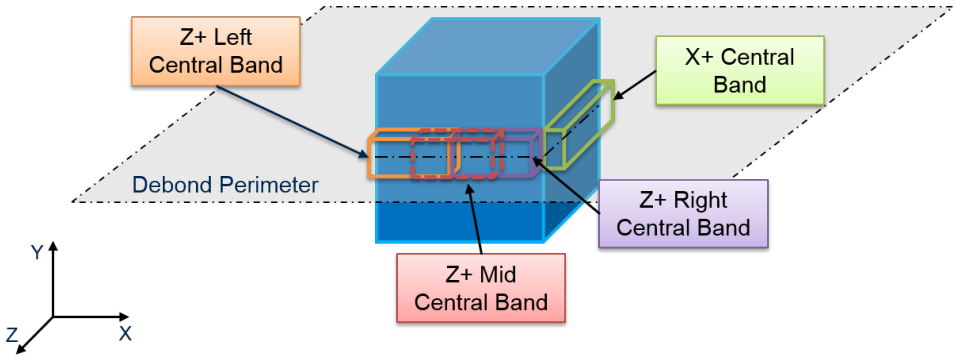

Figure 3.1: Schematic showing the positioning and naming conventions of selected FS AVs with respect to a 50% debonded cuboidal inclusion.

Each of the four distinct volumes shown is replicated on the X^+, X^-, Z^+ and Z^- inclusion faces. The plane labeled *Debond Perimeter* bisects the inclusion along the Y-axis. Matrix elements above this plane are debonded from the inclusion surface by means of a frictionless normal contact, while elements below are bonded via tie constraints. All FIP averaging volumes are bisected by the debond perimeter such that they contain both bonded and debonded elements in equal measure.

Each volume is a rectangular prism of dimensions $W \times H \times T$ where W is the width measured in the plane of the debond perimeter, H is the height along the Y axis and T is the AV thickness measured radially away from the inclusion and perpendicular to the inclusion face. Figure 3.2 gives the measurement conventions for H and T in in reference to the NMI. Here, W is out of the page.

Each AV has $H = 1$ μm and comes in three variants of thickness denoted $T = (t_1, t_2, t_3)$ from smallest to largest as measured perpendicular to the inclusion face.

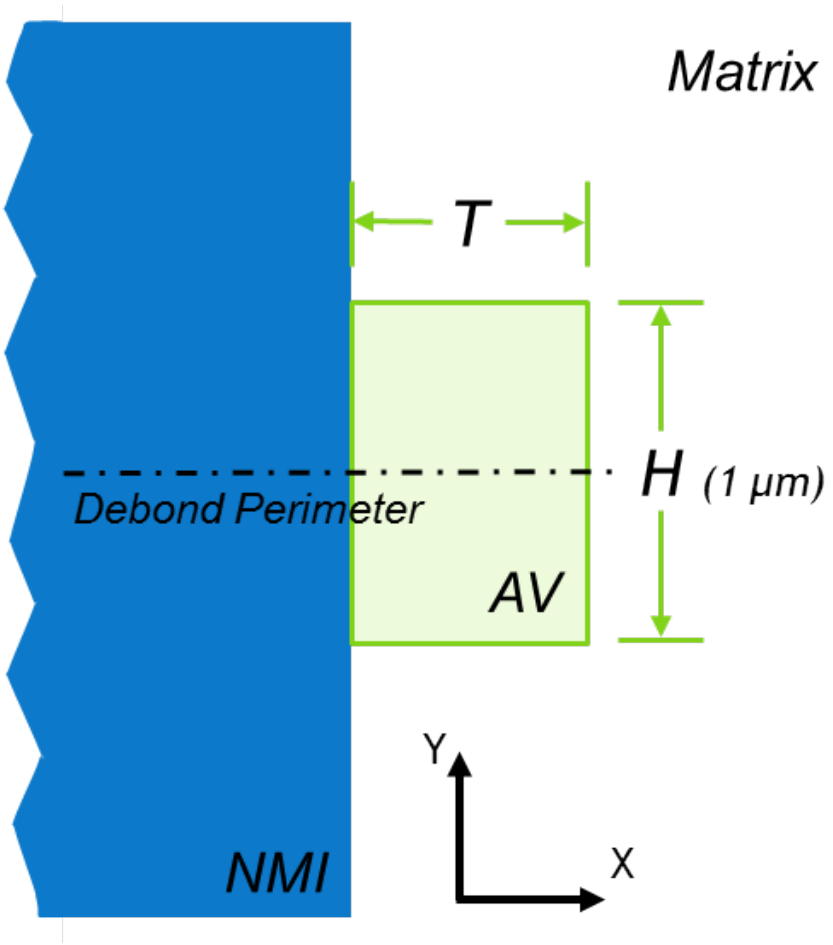

Figure 3.2: Measurement conventions for the FIP AVs with respect to a 50% debonded cuboidal NMI.

Domains denoted by *Full Face* span the width of the inclusion face, while domains *Left*, *Right*, and *Mid* have a width equal to half the inclusion width. The *Mid* domain overlaps both the *Left* and *Right* domains by half. In total, $4 \times 4 \times 3 = 48$ distinct AVs are defined. Table 3.2 lists the volumes of each AV in μm^3 for the case of a 4 μm NMI.

Table 3.2: Volumes (in μm^3) of the FIP AVs for a 4 μm cubic NMI.

AV Identifier	t_1 (0.10 μm)	t_2 (0.25 μm)	t_3 (0.50 μm)
Full Face	0.4	1.0	2.0
Left Face	0.2	0.5	1.0
Mid Face	0.2	0.5	1.0
Right Face	0.2	0.5	1.0

3.4 Extreme Value Statistics

Statistics of extreme values (ie maxima and minima) are useful in the study of the fatigue behavior of engineering components. Engineering components used in life-critical applications must be designed to make the likelihood of fatigue failure extremely small. Prediction of reliability requires characterization of the behavior of the tail end of the population which fails prior to its designed lifespan. Extreme value statistics characterize this tail. Three classes of extreme-value distributions – Gumbel (Type I), Fréchet (Type II) and Weibull (Type III) – can be described by a single distribution through the addition of a shape parameter. This combined distribution is known as the Generalized Extreme Value (GEV) distribution. The cumulative distribution function (CDF) for the GEV distribution is given by

$$F_{\mathrm{GEV}}(x;\mu,\sigma,\xi) = e^{-[1+\xi(\frac{x-\mu}{\sigma})]^{-1/\xi}} \tag{3.10}$$

where μ is the location parameter, σ is the scale parameter and ξ is the shape parameter. Parameters μ and σ are permitted to be any real number, but ξ is restricted to the interval [-1,1]. The shape parameter significantly alters the behavior of the GEV distribution depending on whether $\xi > 0$, $\xi = 0$ or $\xi < 0$. In the case of $\xi = 0$, Eq. 3.10 is undefined and must be replaced by the limit as $\xi \to 0$ resulting in

$$F_{\mathrm{Gumbel}}(x;\mu,\sigma,0) = e^{-e^{(-\frac{x-\mu}{\sigma})}} \tag{3.11}$$

also known as the Gumbel or Type I GEV distribution. In this work, the GEV distribution (Eq. 3.10) is used to fit the distributions of the volume-averaged FS parameter and the corresponding fatigue life correlations. The GEV fit is also compared to the Gumbel distribution fit of Eq. 3.11 for the same data.

3.5 Correlation to Life

Once a sufficiently large sample of the extreme-value FS response values has been constructed from multiple microstructure instantiations, the sample can then be correlated to a life distribution using a modified Tanaka-Mura (T-M) approach [25] [3]. The Tanaka-Mura equation considers that the number of cycles required to incubate a crack along a slip band under HCF loading is related to the energy required to form new surfaces which is inversely proportional to the square of the cyclic plastic shear strain range $\Delta\gamma^p$. By substituting the extreme-value FS parameter for $\Delta\gamma^p$, the following relation emerges [22]:

$$N_{inc} = \frac{\alpha}{d_{gr}}(P_{FS})^{-2} \tag{3.12}$$

where N_{inc} is the number of cycles required to incubate a fatigue crack, d_{gr} is a scaling parameter associated with the microstructural size scale and α is a correlation coefficient, determined by fitting the extreme-value FS distribution to an experimental life distribution.

CHAPTER IV

COMPUTATIONAL IMPLEMENTATION

The CPFEM model developed in this work consists of three main components:

1. A microstructure generation tool that creates the stochastic arrangement of grains within the defined volume;

2. A finite element solver coupling to a physically based constitutive model implemented numerically though a UMAT that iteratively solves for the local stress and strain states;

3. A postprocessing script to extract the local response variables, specifically the volume-averaged Fatemi-Socie Parameter.

This chapter will deal with the implementation of these components within a computational framework including all necessary data inputs and expected outputs. Figure 4.1 provides a summary of the CPFEM model highlighting the flow of information and the necessary software tools for implementation.

The finite element meshes are created with python scripting for ABAQUS, and the grains are assigned via a Matlab [8] script. Each microstructure instantiation undergoes a simulated fatigue loading history in the commercial finite element software package ABAQUS [4]. ABAQUS calls to a custom-built crystal-plasticity User MATerial subroutine (UMAT) implemented in Fortran, which computes the stress-strain response over the entire mesh at each timestep. Prior to analysis, both the microstructure generation tool and the UMAT are calibrated using a combination of experimental data and values from literature. The continuum mechanics basis for the UMAT is presented in Sec 3.2. After the simulated fatigue cycling has been

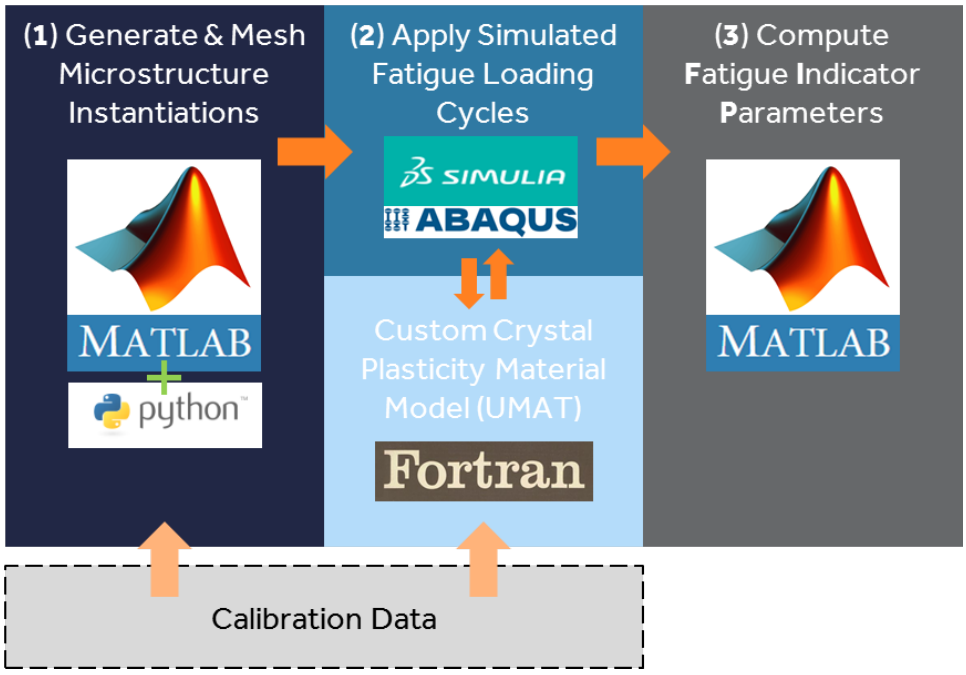

Figure 4.1: Block diagram of information flow through the component parts of the model, showing the software tools used for each step.

completed, a Matlab post-script computes the volume-averaged FS FIPs for each microstructure instantiation based on the local values of the stress and plastic strain tensors.

Once the FIPs have been calculated, the extreme-value FS distribution is populated from the maximum FS value of each microstructure instantiation. The distribution of extreme-value FIPs are then correlated to the distribution of fatigue life values found by experiment though a modified Tanaka-Mura approach as described in Sec 3.5. The fatigue life correlation provides a direct quantitative comparison of the CPFEM model data to experimental fatigue data and can be used to predict fatigue life curves. The following sections provide detailed explanations of the model implementation in the code.

4.1 Microstructure Generation and Meshing

The microstructure is created using an ellipsoid packing algorithm developed by Przybyla [15] and uses a meshing algorithm based on Musinski's work [10]. The target microstructure is a small volume of a MP35N fine-wire matrix surrounding a cuboidal TiN inclusion particle. Since the goal of the model is to examine rare event phenomenon associated with NMIs, the inclusion is input deterministically to each instantiation with full control of inclusion size, position and interface. The loading, interface and boundary conditions around the NMI can all be manipulated to examine their effect on fatigue potency.

4.1.1 User Input Parameters

Table 4.1 summarizes the user input parameters for microstructure generation, along with their default and permissible values. Each input parameter is the name of a variable in the Matlab code which can be set by the user. The input parameters are broken out into six categories: DoE, Geometry, Mesh, Grain Packing, Texture and Loading. The following sections describe the functions of each of the user input parameters by category.

Table 4.1: Independent (user defined) input parameters for microstructure generation

Name	Description	Category	Default Value	Permissible Values
`e_amp`	$n \times 1$ array of strain amplitude values as % of yield strain (ε_y)	DoE	N/A	0.00 to 1.00
`R_num`	$n \times 1$ array of cycle strain ratios ($R = \frac{\varepsilon_{min}}{\varepsilon_{max}}$)	DoE	-1	-1, 0, 0.3, 0.5
`a_r`	$n \times 1$ array of NMI radius (half-width) values in mm	DoE	0.002	0.0005 to 0.005
`run`	$n \times 1$ array of instantiation identifiers	DoE	N/A	positive integers
`d_grn`	Nominal grain diameter in mm. Used to set SVE size	Geometry	0.002	> 0
`geom.O`	NMI origin (centroid) position (X, Y, Z)	Geometry	SVE center	within SVE bounds
`geom.scen`	Integer controlling NMI-matrix interface	Geometry	3	1, 2, 3, 4, 5
`mesh.n_inc_el`	Number of elements to mesh across NMI edge	Mesh	15	9 to 25 (odd only)
`mesh.n_edge_el`	Number of elements to mesh across SVE edge	Mesh	16	10 to 20
`n_grains`	Number of grains to pack in each SVE	Grain Packing	1000	1 to 10000
`Max_Iter`	Maximum allowed grain placement attempts	Grain Packing	10000	≥ 1000
`z_alpha`	1st beta distribution shape parameter (α) to control grain aspect ratio	Grain Packing	7.0	> 0
`w_beta`	2nd beta distribution shape parameter (β) to control grain aspect ratio	Grain Packing	3.0	> 0
`n_Orient`	Number of distinct crystal orientations	Texture	`n_grains`	1 to `n_grains`
`T_frac`	Vector of fractions of each texture component (summing to 1)	Texture	1	0.00 to 1.00
`hkl`	Array of Miller indices defining crystal texture component bins	Texture	[1 1 1]	Miller Indices
`dTheta`	Degrees of variability (2σ) within each texture component	Texture	15	0 to 90
`loadp.e_dot`	Vector of true strain rates for each ABAQUS load step	Loading	1.7×10^{-3}	1×10^{-6} to 1×10^{-3}
`loadp.tmax`	Maximum time (seconds) for each ABAQUS time increment	Loading	0.25	> 0.10
`loadp.e_yield`	0.2 % offset yield strain (ε_y) obtained from tensile test	Loading	0.0102	> 0

4.1.1.1 DoE Parameters

The four DoE parameters `e_amp`, `R_num`, `a_r` and `run`, are used to construct the SVEs necessary to run an arbitrary sized virtual Design of Experiements (DoE). The DoE has three factors associated with strain amplitude (`e_amp`), strain ratio (`R_num`) and NMI half-width (`a_r`). Each factor may have an arbitrary number of levels taking on any of the permissible values as set by the user. At least one SVE is created for every combination of factor levels. The number of microstructure instantiations created at each point in the DoE is determined by the `run` parameter. The `run` parameter is the set of sequential positive integers which provides a unique run ID to each microstructure created. By way of example, the input `e_amp` $= [0.30, 0.45, 0.60]$, `R_num` $= [-1]$, `a_r` $= [0.002]$, `run` $= [1, 2, 3, 4, 5]$ generates five microstructure instantiations at each of three strain amplitudes with $R = -1$ and $r_{NMI} = 0.002$ mm, resulting a total of 15 parameterized SVEs.

4.1.1.2 Geometry Parameters

The geometry parameters `d_grn`, `geom.O` and `geom.scen` control the nominal grain size, NMI centroid position and NMI matrix-interface condition respectively. The SVE edge length is ten times `d_grn` in order to avoid undue influence of a single grain on the SVE mechanical response behavior. The NMI origin (centroid) is set by `geom.O` which is a vector in SVE global coordinates (X, Y, Z). The `geom.scen` parameter is an integer which selects from five preset NMI interface conditions. The five preset interface conditions are (1) completely bonded, (2) Top-only bonded, (3) Upper-half debond, (4) all but bottom debond and (5) solid mesh without NMI. Figure 4.2 illustrates scenarios 2-4 and the resulting stress fields. The red highlighting indicates the mesh regions where tie constraints are applied to create a bonded interface.

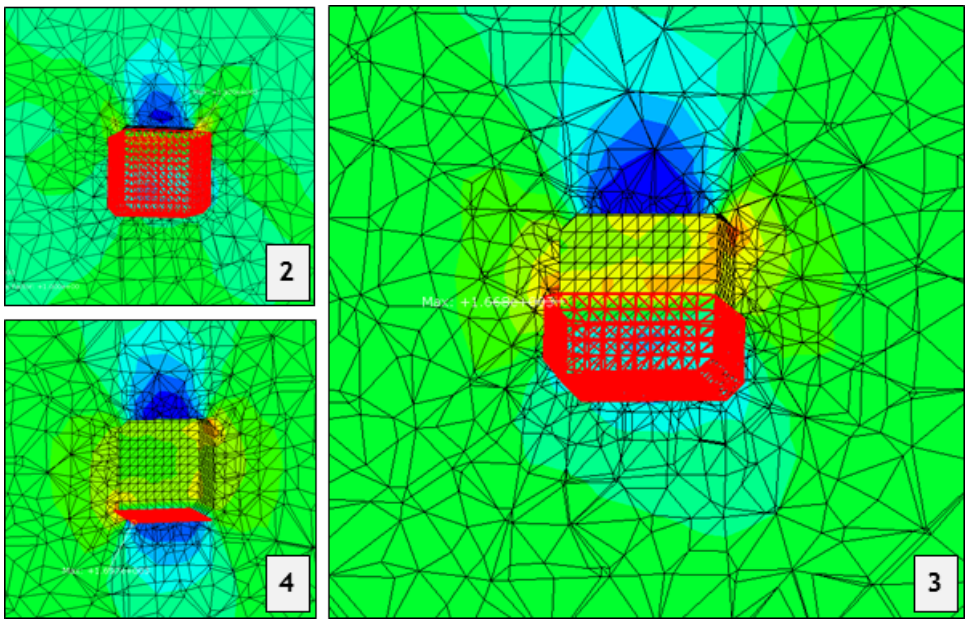

Figure 4.2: Stress-fields around a cuboidal NMI with various interface debonding scenarios. (2) Top-only debond. (3) Upper-half debond (4) All but bottom debond. The NMI has been removed for clarity.

4.1.1.3 Mesh Parameters

The mesh parameters `mesh.n_inc_el` and `mesh.n_edge_el` set the number of elements to mesh across the NMI and the SVE edge respectively. The ratio of these two parameters together with the differences in edge lengths of the NMI and SVE controls the mesh density gradient from the SVE edge to the NMI-matrix interface.

4.1.1.4 Grain Packing Parameters

The grain packing parameters are used to pack each SVE with ellipsoidal grains drawn from distributions of grain size and shape, which are best approximations of experimentally characterized grain size and shape distributions as described in section 2.1.1. The parameter `n_grains` sets the total number of grains to pack in each SVE, while the `Max_Iter` parameter establishes the maximum allowable placement attempts for each grain. The parameters `z_alpha` and `w_beta` are the shape parameters α and β of the beta distribution which is used to control the semi-aspect ratios b/a and

c/a of grain ellipsoids. The beta distribution is defined on the interval $[0, 1]$ and has cumulative distribution function

$$F_\beta(x; \alpha, \beta) = \frac{\mathrm{B}(x; \alpha, \beta)}{\mathrm{B}(\alpha, \beta)} \tag{4.1}$$

where $\mathrm{B}(x; \alpha, \beta)$ is the incomplete beta function defined as

$$\mathrm{B}(x; \alpha, \beta) = \int_0^x t^{\alpha-1}(1-t)^{\beta-1}dt \tag{4.2}$$

and $\mathrm{B}(\alpha, \beta)$ is the beta function, expressed as

$$\mathrm{B}(\alpha, \beta) = \int_0^1 t^{\alpha-1}(1-t)^{\beta-1}dt \tag{4.3}$$

with the requirements that α and β are real numbers greater than zero.

4.1.1.5 Texture Parameters

Texture parameters are used to generate the crystal orientations of the grains to match experimentally characterized texture distributions as described in section 2.1.1. Past studies [10, 15] have employed random grain texture for bulk materials, but the strong fiber texture of MP35N necessitates a reconsidered approach. A new texture algorithm was developed that allows the user to generate SVEs with any number of grain orientation bins weighted by relative frequency in order to approximate texture component by volume-fraction breakdowns from EBSD scans such as that given by Fig 4.3.

The algorithm is best understood by examining the steps involved sequentially:

1. Choose the number of distinct grain orientations to generate using `n_Orient` as well as the number of bins (q) for texture components. The value of `n_Orient` defaults to `n_grains`, but can be made smaller.

2. Select q crystal direction vectors (Miller indices) in the fcc coordinate system to become the center of each texture component bin. The Miller indices are with reference to the global Y axis of the SVE and form the $q \times 3$ array `hkl`.

Sample No	<111>	<001>	<101>	<113>	Total
1	0.589	0.149	0.005	0.239	0.982
2	0.473	0.108	0.025	0.358	0.964
3	0.66	0.199	0.009	0.119	0.987
4	0.655	0.145	0.013	0.167	0.98

Figure 4.3: Volume fraction breakdown of texture components for four different MP35N wire samples with four texture components each. From [7].

3. Define the extent of each bin using `dTheta`, the 2σ angular deviation (in degrees) of a normal distribution centered on the Miller indices in `hkl`.

4. Designate the volume fraction of each texture component relative to the whole using the $q \times 1$ array `T_frac`. The i^{th} entry in `T_frac` corresponds to the i^{th} Miller index in `hkl` and the summation of all entries in `T_frac` must be unity.

5. Bin the total number of distinct grain orientations to be generated into the q crystal texture bins by multiplying each of the elements in `T_frac` by `n_Orient`.

6. Generate the appropriate number of individual grain orientations (expressed as crystal direction vectors) for each bin by sampling from the normal distributions of each Miller index in `hkl`.

7. Express each individual crystal direction vector in Euler angles (ϕ_1,Φ,ϕ_2) in the Bunge convention.

4.1.1.6 Loading Parameters

The loading parameters are used together with the `e_amp` and `R_num` parameters to define the loading profile to apply to each SVE. The `loadp.e_dot` parameter defines the true strain rate to use at each ABAQUS load step. The `loadp.tmax` parameter establishes the maximum allowable time for an ABAQUS time increment, and the

`loadp.e_yield` parameter provides the 0.2% offset yield strain as obtained from tensile tests. Unlike the DoE parameters, the Load parameters remain unchanged between successive SVEs.

4.1.2 Instantiation of Statistical Volume Elements

An SVE is instantiated by generating a block of tetrahedral mesh containing an NMI surrounded by a crystal-plasticity region. The crystal plasticity region is subsequently packed with ellipsoidal grains by assigning distinct materials to ellipsoidal element subsets of the CP region. The location, size, semi-axes ratios and physical orientation of these ellipsoids are controlled by an ellipsoidal grain packing algorithm. This algorithm was developed by Przybyla [15] and modified to work with tetrahedral elements. A cut-section view of an exemplary microstructure instantiation is shown in Figure 4.4. The grain packing algorithm consists of the following steps:

1. **Determine the number of grains to pack.** The total number of grains packed depends on the size of the SVE and the grain size distribution established.

2. **Assign a target volume to each ellipsoidal grain.** The target volume of each ellipsoid is obtained by converting the grain diameter value sampled from the experimental grain diameter distribution. The conversion equation is $V_{target} = \frac{4\pi}{3}(\frac{d_{grn}}{2})^3$.

3. **Scale each target volume to a packing volume.** The target volume is the idealized volume for the completely packed SVE. It is impossible to perfectly pack a volume with ellipsoids without overlap. Therefore each volume is scaled down by a factor to account for imperfect packing.

4. **Sort the list of ellipsoid grain volumes in descending order.** For greatest packing efficiency, the largest ellipsoid is packed first.

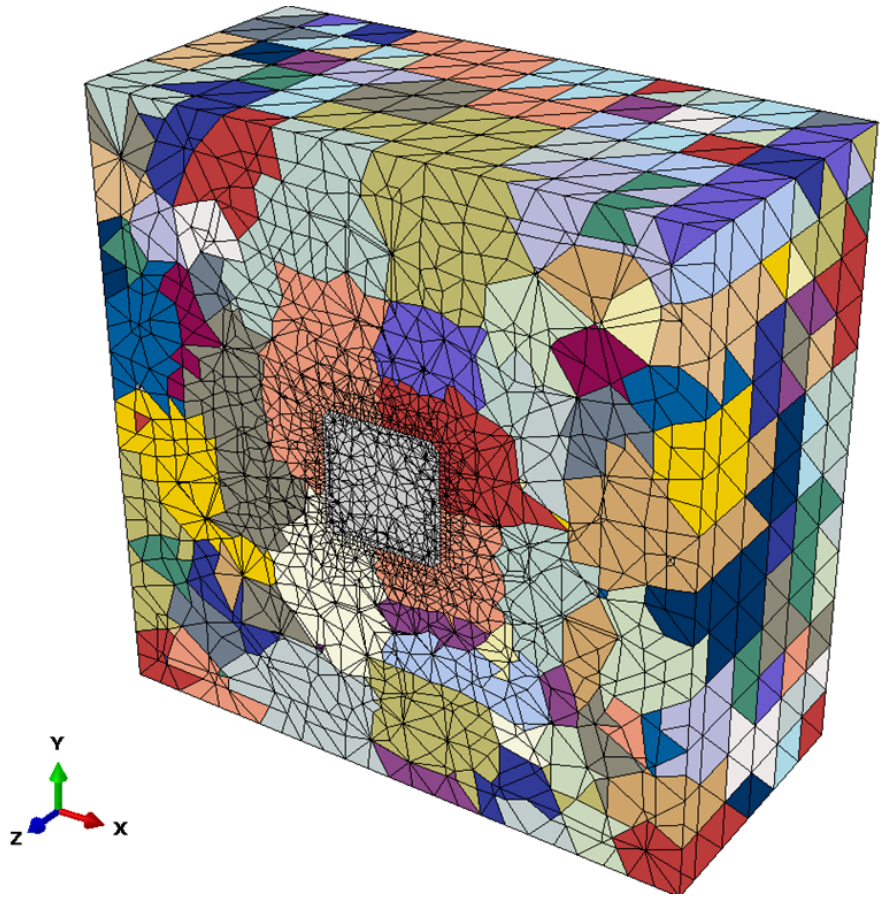

Figure 4.4: Cut-section view of an exemplary microstructure instantiation with 1000 grains. Grains are delineated by color. The cuboidal TiN NMI particle is shown in grey in the center. The width of the NMI is 4 μm and the SVE is 20 μm on each side.

5. **Assign ellipsoid shapes.** Ellipsoid morphologies are defined by the semi-axis ratios b/c and c/a. These axes ratios are sampled from a beta distribution which is a best estimate of MP35N grain morphology since experimental grain aspect ratio data was unavailable. The beta distribution parameters are discussed in Sec 4.1.1.4.

6. **Assign crystal orientation.** Each grain is assigned a set of Euler angles in Bunge convention (ϕ_1, Φ, ϕ_2) based on the output of the texture generation algorithm in section 4.1.1.5 defining the crystals rotation from the global coordinate axes. This is unrelated to the semi-axes orientation.

7. **Seed an ellipsoid into the SVE.** Ellipsoids are placed in decreasing order of volume to maximize packing efficiency. A random seed point (X_0, Y_0, Z_0) within the bounds of the SVE is chosen as the ellipsoid centroid. At the same time, a random orientation of the semi-axes is picked.

8. **Check for grain overlap.** The newly placed ellipsoid must not overlap with any previously packed grains. To check this, it is required that every element within the ellipsoid boundary R_b is unassigned. If overlap occurs, a new random seed point is chosen.

9. **Assign elements to current grain.** If no elements within R_b are previously assigned, the space is available. All elements inside R_b are assigned to the current grain.

10. **Repeat steps 7-9** until all ellipsoids have been placed or the jamming limit is reached. The jamming limit sets the number of grain placement attempts allowed for a single grain. If this limit is reached and not all grains have been placed, the algorithm quits because not enough empty space remains to finish grain placement.

11. **Grow grains until all CP elements are assigned.** At this point, all ellipsoids have been placed, but some unassigned elements remain between them. To fill the SVE volume, these remaining elements are assigned to their nearest grains. In this way, the grains "grow" uniformly to fill the SVE.

A 2-dimensional illustration of the grain placement scheme, and associated coordinate systems used is shown in Figure 4.5. As long as the element centroid falls within the ellipsoid boundary R_b, it is considered to belong to the current grain.

As stated, the grain packing algorithm attempts to match an experimental grains size distribution. Because of the domain discretization imposed by the finite element

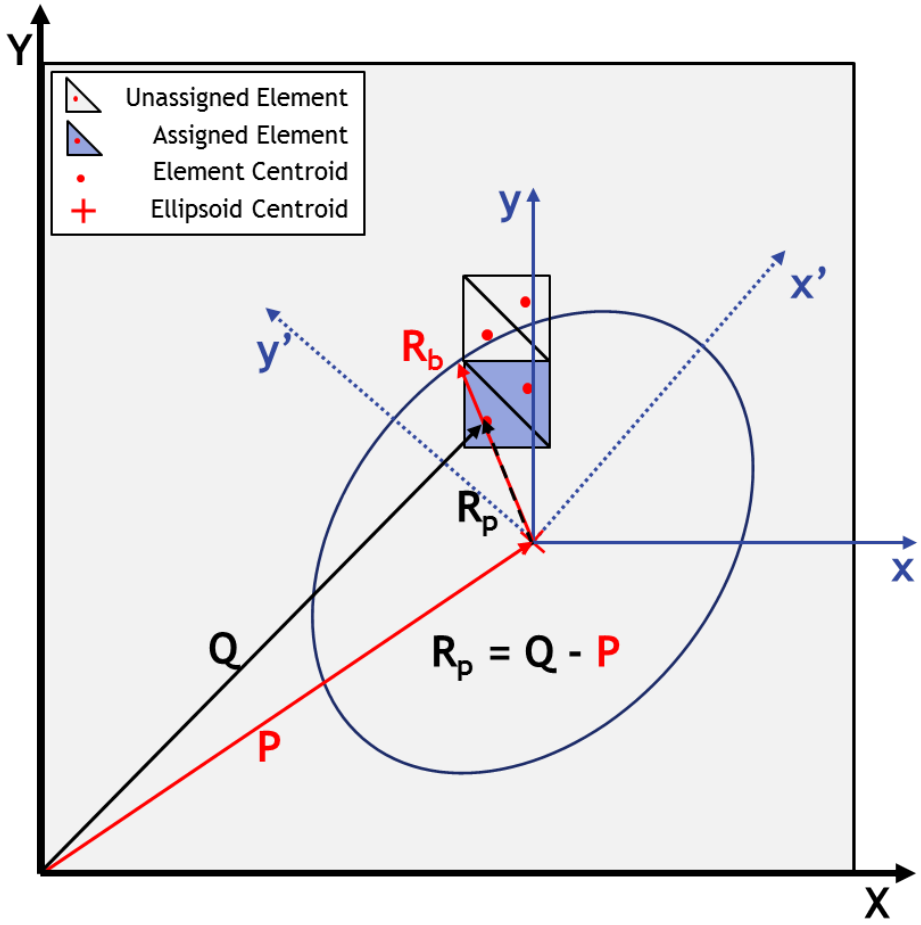

Figure 4.5: 2D illustration of ellipsoid grain placement showing coordinate systems and naming conventions used. For clarity, only a few elements are shown, and the inclusion is excluded.

mesh an exact match of the experimental distribution is not possible. However, a reasonably close match can be obtained, provided by the appropriate number of grains are input. Figure 4.6 compares the achieved grain size distribution to the target distribution for a representative microstructure instantiation with 1000 grains. The achieved distribution falls short of the target distribution for grains with volume $V_{grn} \leq 0.5 \times 10^{-8}$ mm^3 and exceeds it for grains with volume $0.5 < V_{grn} \leq 1 \times 10^{-8}$ mm^3. This shifted grain size distribution is consistently present in all 1000 grain SVEs with a volume of 20 μm^3. Grains with volumes below 0.5×10^{-8} mm^3 are undesirable from a mesh quality standpoint since it means the grain consists of only

a handful of elements.

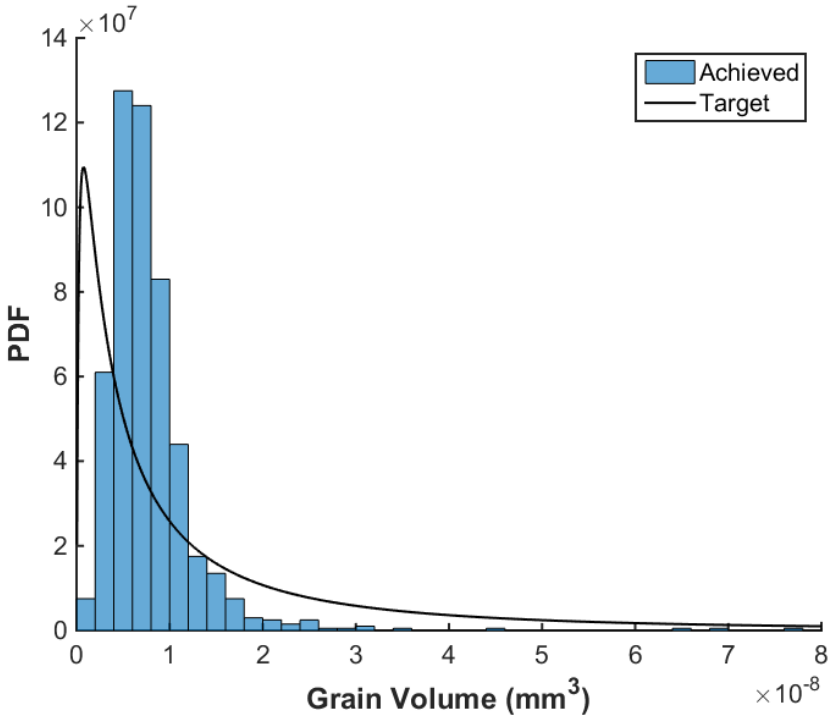

Figure 4.6: PDF of a representative microstructure instantiation with 1000 grains comparing the achieved grain size distribution to the target distribution.

Grain morphology of the ellipsoids are specified by the ratios b/a and c/a, where a, b, c are the semi-axes of the ellipsoid, satisfying $a > b > c$. These axes ratios are taken from a beta distribution which is a best estimate of actual MP35N grain aspect ratios since experimental grain aspect ratio data is not available. The values of the shape parameters α and β used in the beta distribution are listed in Table 4.1. A point cloud of the targeted semi-axes ratios from an exemplary 1000 grain microstructure instantiation is presented in Figure 4.7. All points lie below the line $b/a = c/a$ since $b > c$ in all cases. Actual semi-axes ratios may deviate slightly from the targets due to the grain growth step.

4.1.3 Mesh Quality Study

The finite element mesh utilized in this model is comprised of linear tetrahedral continuum elements (C3D4). These elements permit mesh refinement around areas of

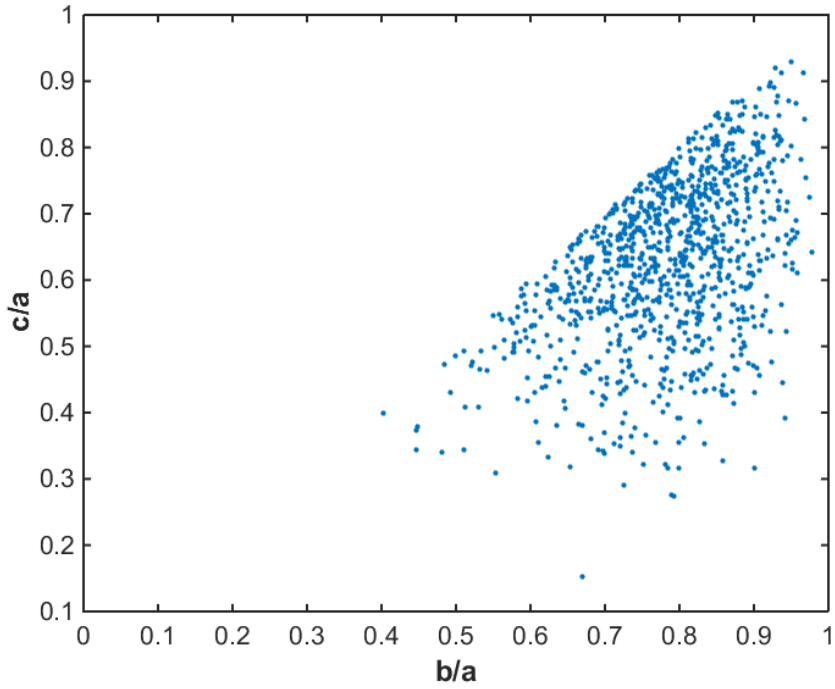

Figure 4.7: Targeted grain semi-axes ratios of a representative microstructure instantiation with 1000 grains.

high stress concentration. However, they exhibit slow convergence with decreasing mesh size, being linear with a single integration point. A study was conducted to assess the influence of mesh size on the volume-averaged FS response, and to determine the minimum level of mesh refinement around the NMI necessary to achieve a converged response. A mesh test microstructure block was constructed in order to isolate the effect of mesh refinement from the effects of grain placement and texture. The mesh test block features 64 cubic grains arranged in a $4 \times 4 \times 4$ grid layout with a 4 μm half-debonded cubic NMI in the center. Figure 4.8 shows a cut-section view through the Z midplane of the mesh test block, with individual grains being demarcated by color.

There are 8 grains adjacent to the NMI, which is debonded from the matrix above the Y midplane, meaning that the upper 4 grains are disconnected from the NMI. The mesh quality study examined 8 levels of mesh refinement corresponding to increasing

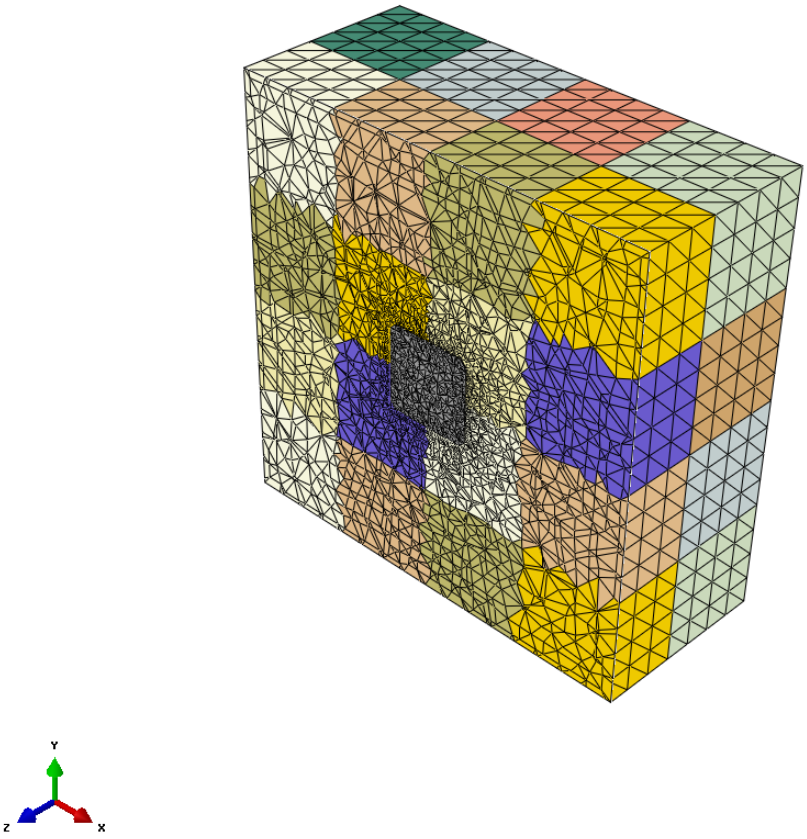

Figure 4.8: Cut-section view of SVE generated for mesh quality study showing 64 cubic grains and central NMI.

the number of elements along the NMI edge. Table 4.2 shows the mesh densities, model size and run times for each of the 8 mesh density levels. The model size is the total number of elements present in the model and is the sum of the matrix and NMI elements. All mesh instantiations are evaluated over the third fully-reversed tension-compression cycle with a loading amplitude of $0.55\,\varepsilon_y$ to ensure non-zero plastic strain values within the FS AVs. Grains retain the same position, size and crystal orientation for all mesh density levels.

The mesh is most dense at the NMI edge and gradually becomes coarser towards the SVE boundary. As the number of elements along the NMI increases, the model size also increases, resulting in an increase in the run time. Figure 4.9 shows the time to run the model for increasing mesh density. The models were run in a Linux

Table 4.2: Summary of size and run-time measures for the eight mesh density levels

Mesh Density Level	Elements along NMI Edge	Elements along SVE Edge	Model Size	Matrix Model Size	Run Time (s)
1	9	12	27,924	24,880	1,513
2	11	12	34,951	29,987	1,924
3	13	16	62,235	54,054	3,533
4	15	16	78,184	66,871	4,585
5	17	16	89,012	73,718	5,204
6	19	16	99,395	79,122	7,140
7	21	20	144,947	120,027	11,193
8	25	20	169,320	131,036	21,935

high-performance computing environment utilizing parallel processing on a total of 40 CPUs. A mesh density of 17 elements along the NMI can be considered a transitional value for computational efficiency. Above this value, the run-time begins to increase rapidly, while below it the run-time increases slowly and stays below 5000 seconds. Based on this data, it is seen that higher computational efficiency is achieved using a mesh density at or below 17 elements along the NMI edge, so long as the volume-averaged FS values using that mesh density can be considered converged.

Convergence of FS values can be evaluated by comparing the change in FS values as mesh density is increased. Figure 4.10 shows the FS response of the Full-Face AV along the $X-, X+, Z-, Z+$ NMI faces against the number of elements along the NMI edge which can be thought of as the linear element density. The AV located along the $Z-$ face showed an elevated FS response compared to the other three faces, due to higher levels of plasticity resulting from grains oriented favorably for slip. The other three face volumes have nearly identical response values to one another. The $Z-$ Face AV and the others share a similar response profile as mesh density is increased,

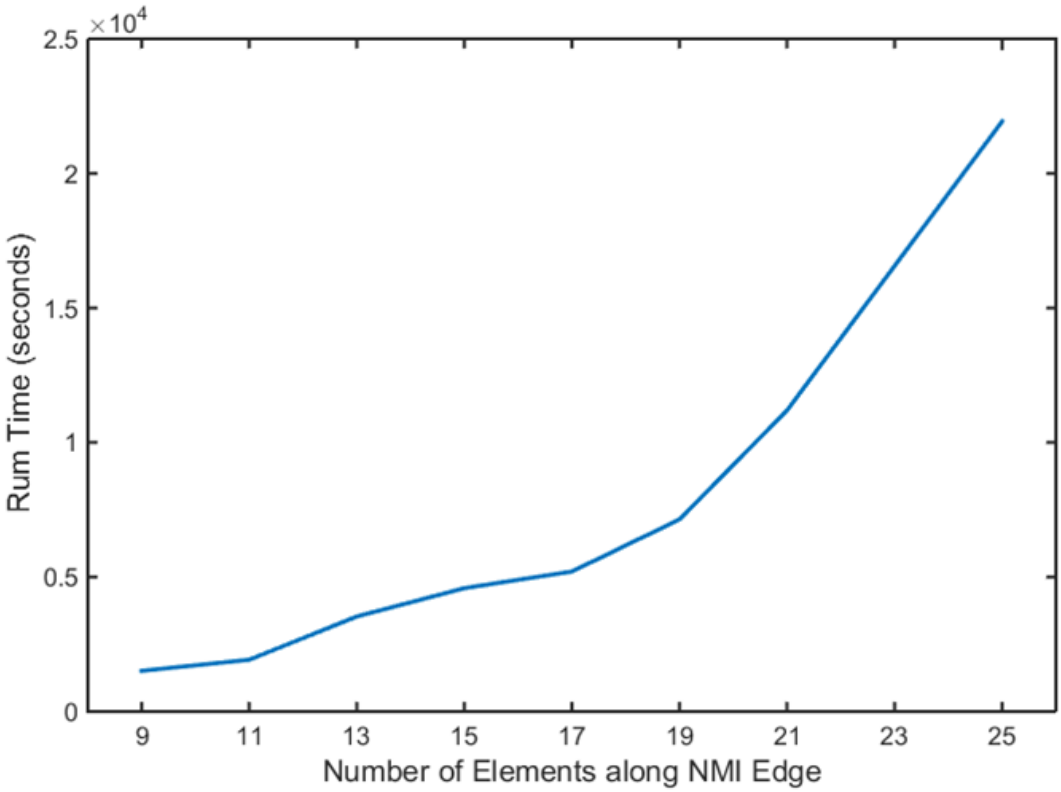

Figure 4.9: Run-time (in seconds) for increasing number of elements along NMI edge.

however the profile is exaggerated for the $Z-$ Face AV due to the intensified FS response there. Between 9 and 11 the FS response is essentially unchanged. From 11 to 15, the FS response increases sharply by 50% from 0.8×10^{-3} to 1.2×10^{-3}. Above 15, the FS response value stabilizes, rising only 13% over a linear element density increase of 10. Based on this analysis, the FS response for the Full-Face AVs were considered converged at a linear NMI density of 15 elements.

The FS value convergence response was also checked on the Mid AV to confirm the smaller AVs with one-half NMI width behaved similarly. Figure 4.11 shows the FS response of the Mid AV along each of the $X-, X+, Z-, Z+$ NMI faces, plotted on the same axes as Figure 4.10. The $Z-$ Mid-Face AV response has been translated upward by roughly 0.2×10^{-3} compared to the Z- Full-Face AV while maintaining a similar profile shape. As in Figure 4.10, the FS response value rises between 11 to

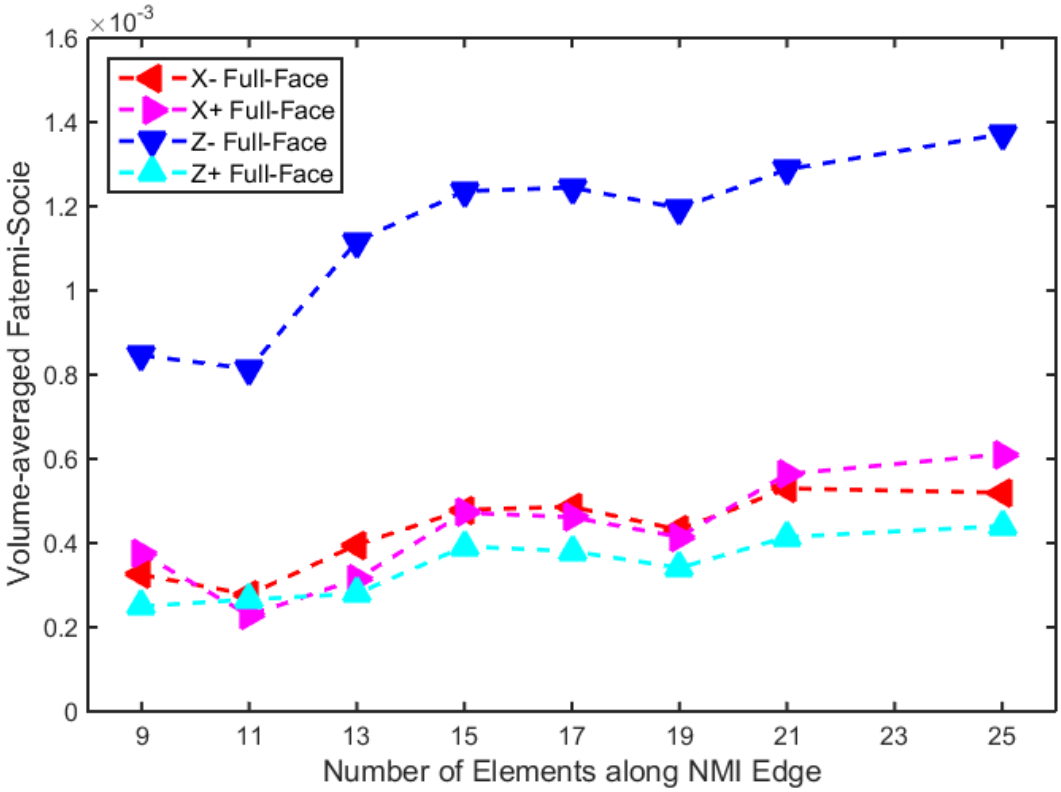

Figure 4.10: Volume-averaged Full-Face FS response for increasing number of elements along NMI edge.

15 and flattens out at higher densities. The other three Mid-Face AVs responses are nearly unchanged compared to their Full-Face counterparts. Because of this, a mesh density of 15 elements along the NMI edge was the mesh density selected for use in further studies, being the minimum mesh density needed for converged FS response values.

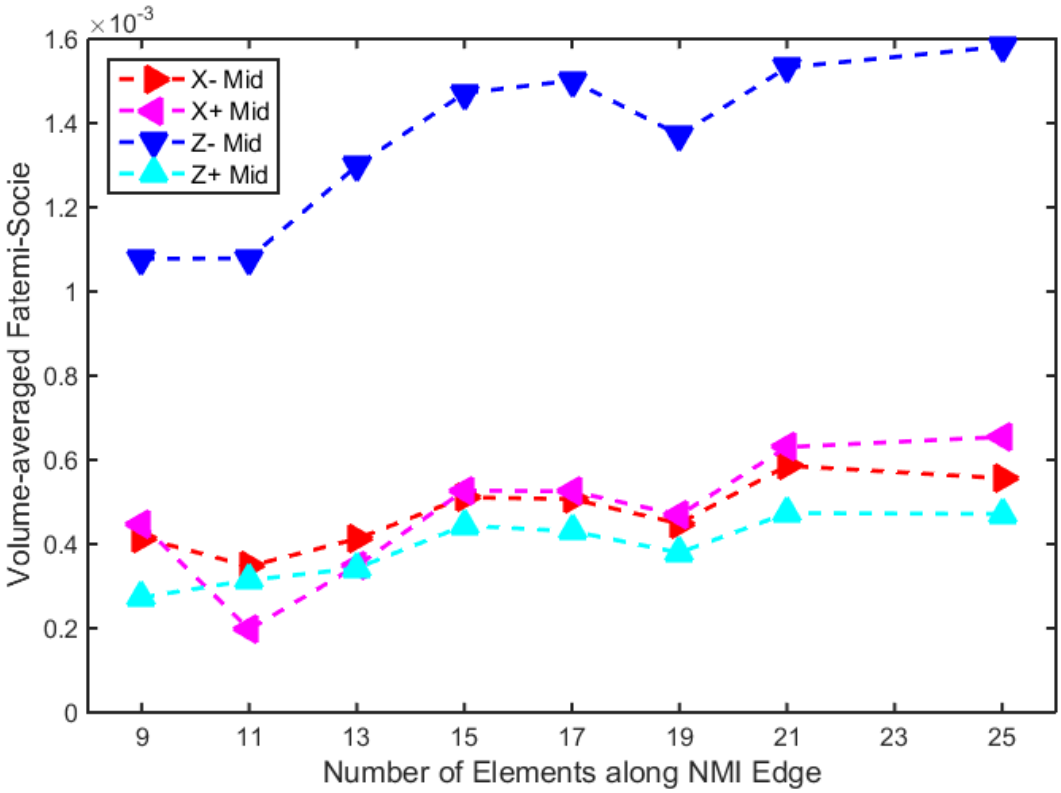

Figure 4.11: Volume-averaged Mid-Face FS response for increasing number of elements along NMI edge.

Table 4.3: Variables, parameters and coefficients used in constitutive relations

Type	Name	Symbol	UMAT equivalent	Description
index	slip-system	α	`n` or `k`	Crystal slip-system identifier. Ranges from 1-12 for octahedral systems.
variable	shear strain rate	$\dot{\gamma}$	`gamma_dot`	Inelastic shear strain rate
coeff.	shear rate coeff.	$\dot{\gamma}_o$	`gamma_dot_zero`	Inelastic shear strain rate coefficient
variable	resolved shear stress	τ	`tau`	Resolved shear stress.
variable	backstress	χ	`a`	Internal, kinematic stress which results from pile-up of dislocations along grain or other boundaries.
variable	threshold stress	κ	`g`	Isotropic stress that controls the onset of inelastic deformation.
phys. param.	drag stress	D	`d`	Stress governing internal resistance to plastic flow.
phys. param.	flow exponent	n	`flow_exp1`	Exponent governing the material strain-rate sensitivity.
phys. param.	initial threshold stress	κ_o	`tau_0`	Initial threshold stress value.
coeff.	dislocation arrangement coefficient	α_t	`alpha`	Coefficient to account for dislocation arrangement in microstructure.
phys. param.	shear modulus	μ	`pmeu_matrix`	Shear modulus of MP35N.
phys. param.	Burger's vector	b	`c_b`	Burger's vector magnitude for MP35N.
variable	dislocation density	ρ	`rho`	Dislocation density on a given slip-system.

4.2 Constitutive Model Parameter Fitting

The parameters of the constitutive model outlined in Sec 3.2 were calibrated using a combination of existing values from literature, first principles calculations, and iterative fitting against cyclic mechanical test data. The material response is a function of both the parameter values and the crystallographic texture of the microstructure, so the parameter fits must be adjusted for significant changes in texture. Three distinct model calibrations were performed: an initial calibration that was a first-order approximation targeting a microstructure with a single texture distribution around the $\langle 111 \rangle$, an intermediate calibration to improve the kinematic hardening response and a revised calibration targeting a microstructure with multiple texture components in the $\langle 001 \rangle$, $\langle 113 \rangle$ and $\langle 111 \rangle$. The parameter fitting for the initial, intermediate and revised calibrations as well as the calibration experiments undertaken are described in the following sections.

4.2.1 Calibration Experiments

Data from two main calibration experiments was collected on MP35N fine wire in order to appropriately fit the constitutive model parameters to the material response behavior. In order to calibrate the isotropic hardening behavior and the strain-rate sensitivity, uniaxial tensile test data was collected from [14]. This test was conducted on a 10 in length of low-Ti as-drawn MP35N wire in displacement control alternating every 0.5% strain between high and low strain rates of 1.7×10^{-3} and 1.7×10^{-5} s^{-1} respectively. Figure 4.12 shows the stress-strain plot for the so-called strain-rate jump test illustrating the jump test. The sensitivity of the stress response to the strain rate becomes evident beyond 1% strain when the wire response is no longer purely elastic.

The parameters governing the kinematic hardening behavior were determined by fitting to the model to cyclic tension-tension experiments. Two 10 in lengths of low-Ti MP35N as-drawn wire were cycled in load control for 10,000 cycles under a

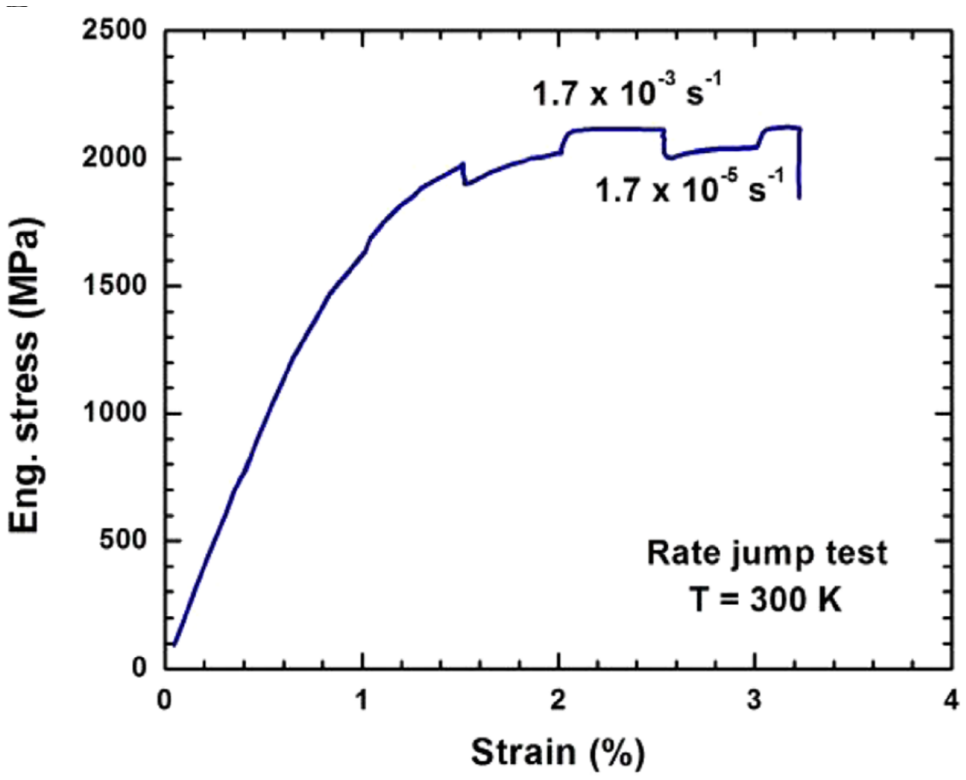

Figure 4.12: Strain-rate jump test on low-Ti MP35N as-drawn wire with strain rate alternating every 0.5% increment of strain. From [14].

$R = \frac{S_{min}}{S_{max}} = 0.5$ load ratio. The tests had different maximum stress values of ${S_{max}}^1 =$ 1400 MPa and ${S_{max}}^2 = 1500$ MPa referred to as LCF1 and LCF2, respectively. After hundreds of cycles, the difference in accumulated strain between the two tests caused by the non-zero mean stress could be compared to determine the increment of strain over each cycle. Figure 4.13 shows the results of the first 300 cycles of each test.

The total accumulated strain for LCF 2 is larger than for LCF 1. To determine the rate of plastic strain accumulation, the peak strain values for LCF 1 are plotted against the base-10 log of cycles $\log(N)$ as shown in Figure 4.14. Each data point is the peak strain over a single cycle. The rate of strain accumulation stabilizes to a logarithmic relationship after ten cycles. A similar logarithmic fit was calculated for LCF 2. The difference in strain accumulation between LCF 1 and LCF 2 was used to calibrate the backstress evolution parameters.

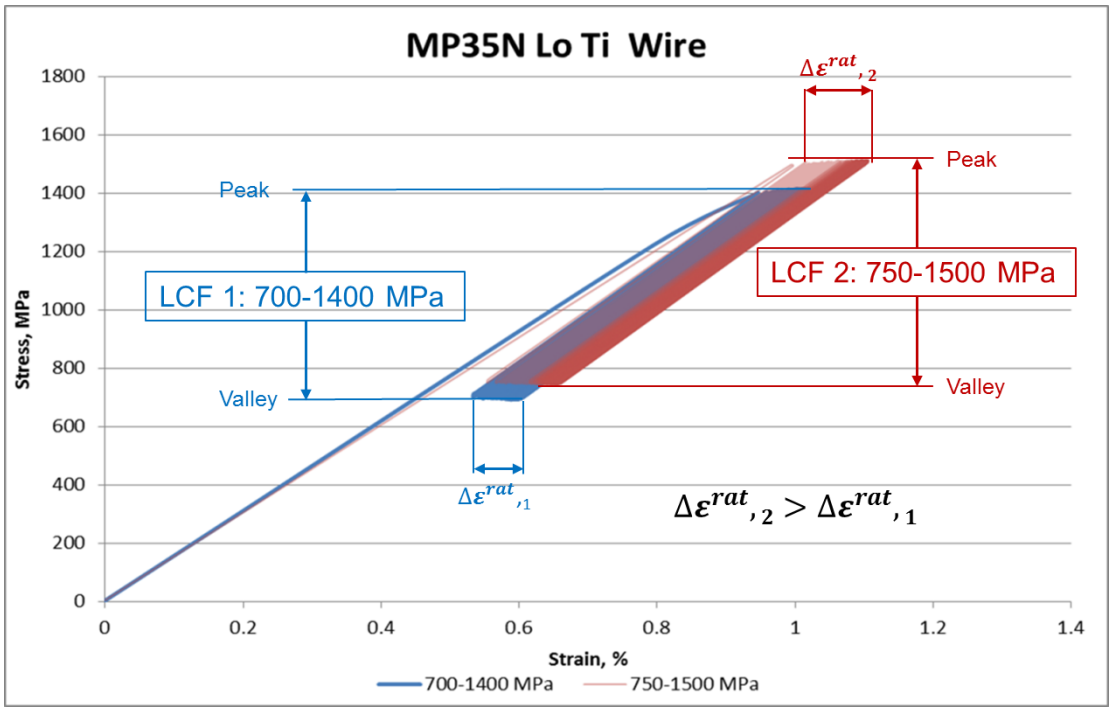

Figure 4.13: Strain Ratcheting Experiments showing the accumulation of strain over 300 cycles for ${S_{max}}^1 = 1400$ MPa and ${S_{max}}^2 = 1500$ MPa.

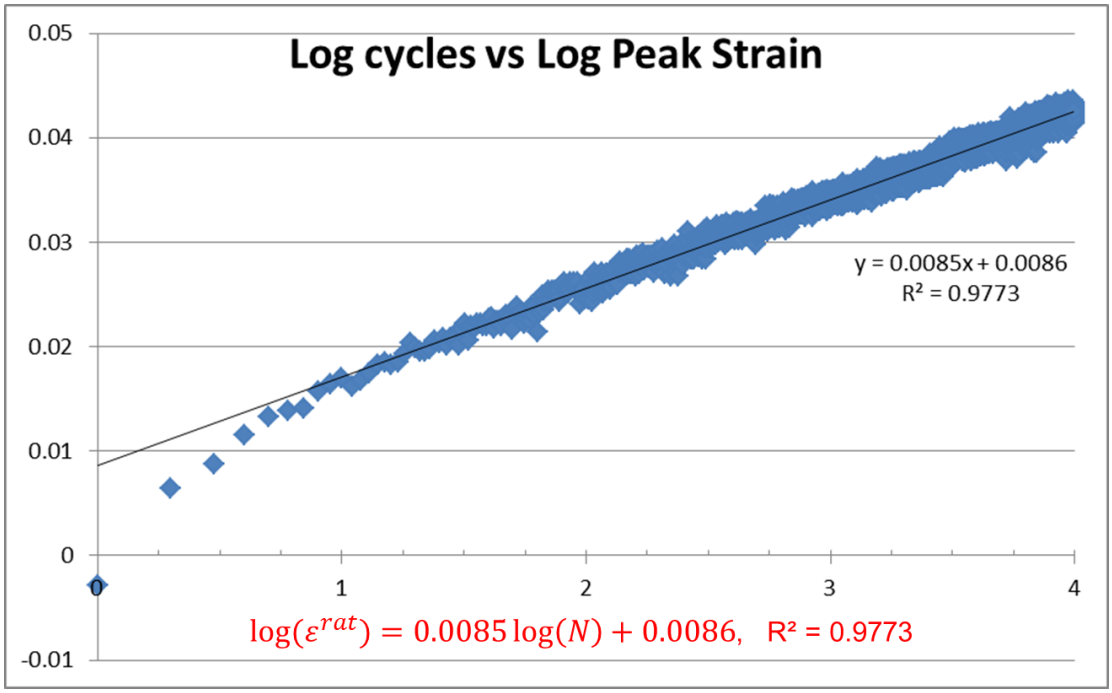

Figure 4.14: Plot of $\log(N)$ vs peak strain (mm/mm) for the LCF1 experiment. The rate of strain accumulation stabilizes after 10 cycles.

4.2.2 Initial Parameter Calibration

The initial model calibration was a first order estimate targeting a microstructure with a single texture component distribution around the ⟨111⟩ orientation. The parameter values for the initial calibration are given in Table 4.4.

Table 4.4: Values of the constitutive parameters for the initial model calibration (UMAT v28)

C_{11}	C_{12}	C_{44}	$\dot{\gamma}_o$	n	D_o	τ_o	ρ_o
179,789 (MPa)	89,485 (MPa)	70,285 (MPa)	6.1×10^{16} (s^{-1})	15	150 (MPa)	85.15 (MPa)	7.0×10^9 (mm^{-2})
α_t	μ	b	n_k	c_{gr}		d_{gr}	f_{tw}
0.1	70,285 (MPa)	0.407 (nm)	1	9.432 ($MPa\sqrt{mm}$)		0.002 (mm)	0.1
C_χ	η_o	t	h_o	k_1	k_2	k_3	
2	2.82	0.0001 (mm)	0.4	100,000 (mm^{-1})	3.162	0.1	

Parameters n, D_o, τ_o, α_t, b, n_k, c_{gr}, C_χ, η_o and h_o are unchanged from the values in [21] used for IN100. The values of these parameters for MP35N are expected to be similar to those for IN100, since both are fcc alloys containing significant Ni content. Parameters d_{gr}, f_{tw}, t and k_3 were added to account for the strengthening effect of the small grain size and nano-scale twins. The value of d_{gr} was set to the median grain size of 2 μm and t was given a value of 10 nm consistent with the twin spacing revealed by TEM [14, 23]. The values of f_{tw} and k_3 were chosen to reflect physically reasonable values. The shear strain rate coefficient $\dot{\gamma}_o$ is set to 6.1×10^{16} s^{-1}. The initial dislocation density ρ_o was given a value of 7.0×10^9 mm^2 reflecting the high initial dislocation density from 36% cold work in the as-drawn MP35N wire. Additional cyclic deformation from fatigue type loading is not expected to further increase ρ, so the ratio of k_1 and k_2 is selected such that ρ saturates above ρ_o.

The values of the elastic parameters C_{11}, C_{12} and C_{44} needed for the 4th rank

elastic stiffness tensor **C** were established by density functional theory (DFT) using a calculation methodology derived from the technique in Wang et al. [26] since values for MP35N were not available in literature. A non-linear weighted average interpolated between values of elastic constants found for pure fcc Ni, Co, Cr, Mo and binary alloys Ni-31Co, Ni-31Cr and Ni-31Mo. The results are presented in Table 4.5.

Table 4.5: Results of DFT atomistic calculations for Ni-35Co-20Cr-10Mo alloy calculated at 0 Kelvin (ShunLi Shang, personal communication, 14 August 2013).

Alloy Composition	$\mathbf{C_{11}}$ (GPa)	$\mathbf{C_{12}}$ (GPa)	$\mathbf{C_{44}}$ (GPa)	**Volume** ($\AA^3$/atom)
fcc Ni	279.2	160.1	130.6	10.917
fcc Co	296.6	171.9	144.0	10.901
fcc Cr	110.7	241.5	-36.5	11.917
fcc Mo	120.9	305.1	13.7	16.195
fcc Ni31Co	279.9	156.0	130.9	10.915
fcc Ni31Cr	280.5	160.2	130.1	10.925
fcc Ni31Mo	276.6	162.5	123.5	11.053
fcc Ni-35Co-20Cr-10Mo	**280.92**	**139.82**	**109.82**	**11.263**

Based on these values of the elastic constants, the anisotropy ratio of MP35N can be calculated as

$$A = \frac{2\mathrm{C}_{44}}{\mathrm{C}_{11} - \mathrm{C}_{12}} = 1.56 \tag{4.4}$$

The theoretical calculation of the elastic coefficients C_{11}, C_{12}, and C_{44} for 0 Kelvin given in Table 4.5 resulted in an effective elastic modulus that was too high when compared to uniaxial tensile tests conducted at ambient temperature. In order to improve the elastic modulus fit, the values of all elastic coefficients were scaled by a factor of 0.64. The resulting values retain the same anisotropy ratio as Eq. 4.4 and are provided in Table 4.4.

4.2.3 Intermediate Parameter Calibration

An intermediate calibration was undertaken to improve isotropic and kinematic hardening behavior of the model to the monotonic tensile and cyclic tension-tension tests. Several parameters were adjusted from the initial fit of Table 4.4 including $\dot{\gamma}_o$, n, D_o, τ_o, ρ_o, η_o and the elastic constants. The adjusted parameter values used in the intermediate calibration are given in Table 4.6. Comparisons of the model fits using the initial and intermediate model calibrations against the strain-rate jump and LCF 1 experiments are provided in Figures 4.15 and 4.16, respectively. In these plots, the terms "original" and "latest" refer to the initial and intermediate parameter calibrations.

Table 4.6: Values of the constitutive parameters for the intermediate model calibration (UMAT v110)

C_{11}	C_{12}	C_{44}	$\dot{\gamma}_o$	n	D_o	τ_o	ρ_o
165,406 (MPa)	82,326 (MPa)	64,662 (MPa)	7.2×10^{16} (s^{-1})	18	195 (MPa)	75.15 (MPa)	3.0×10^9 (mm^{-2})
α_t	μ	b	n_k	c_{gr}		d_{gr}	f_{tw}
0.1	64,662 (MPa)	0.407 (nm)	1	9.432 ($MPa\sqrt{mm}$)		0.002 (mm)	0.1
C_χ	η_o	t	h_o	k_1	k_2	k_3	
2	68.0	0.0001 (mm)	1	100,000 (mm^{-1})	1.0	0.1	

An increase of the flow exponent n from 15 to 18 improves the rate sensitivity of the model as evidence by the deeper trough features in the "latest" model fit. The amount of isotropic hardening seen post-yield is also increased by enhancing the value of η_o to better reflect the experiment. The value of the elastic coefficients C_{11}, C_{12} and C_{44} are reduced proportionately from the initial fit, resulting in a poorer fit of the elastic portion of the curve. This reduction was a compromise in order to better fit the cyclic value of the elastic modulus in Fig 4.16. In this plot, the first

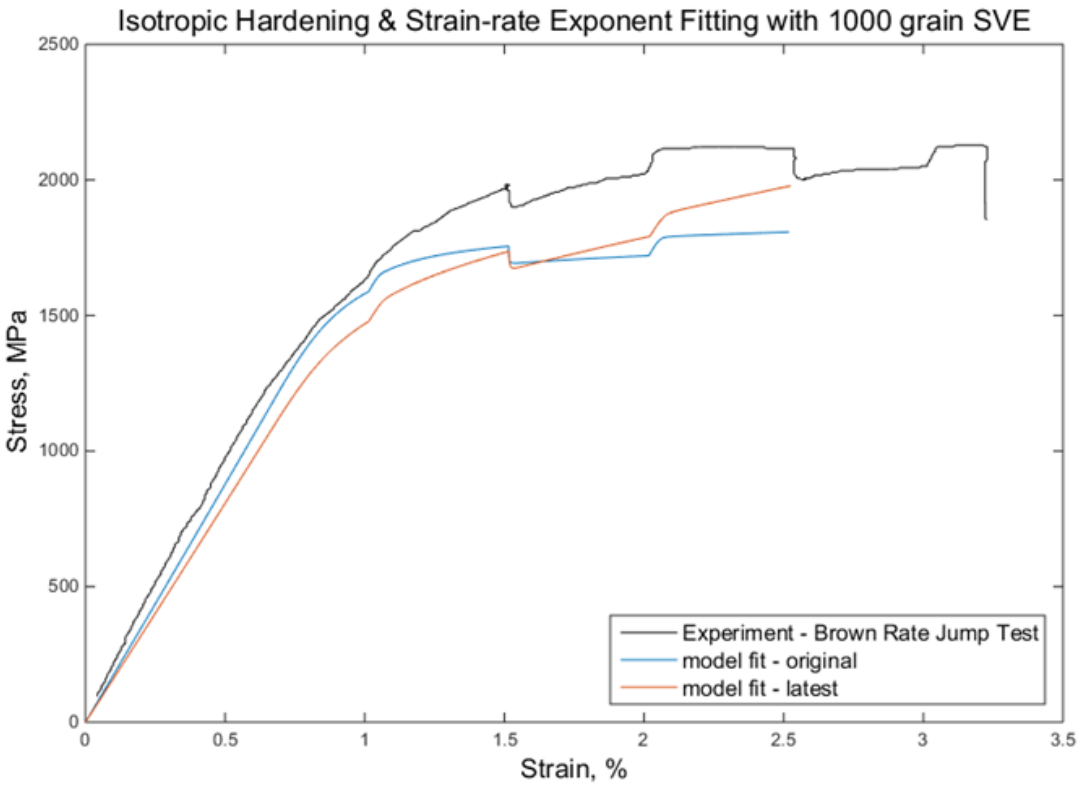

Figure 4.15: Comparisons of the initial and intermediate parameter calibrations to the rate jump uniaxial tension test. Experimental data from [14].

300 cycles of the LCF 1 experiment have been plotted, together with fits for the initial and intermediate parameter calibrations. The model fits extend to 24 cycles. The model fit from the intermediate parameter calibration shows improved fits for the cyclic portion of the data past the initial load in terms of the amount of strain accumulation over a cycle.

4.2.4 Revised Parameter Calibration

A third calibration of the constitutive model parameters was conducted targeting a microstructure with multiple texture components. The parameter values for the revised model calibration are given in Table 4.7.

The values of the elastic coefficients have been enhanced from the initial fit to 0.85 from the theoretical values computed for 0 Kelvin. This adjustment was necessary to

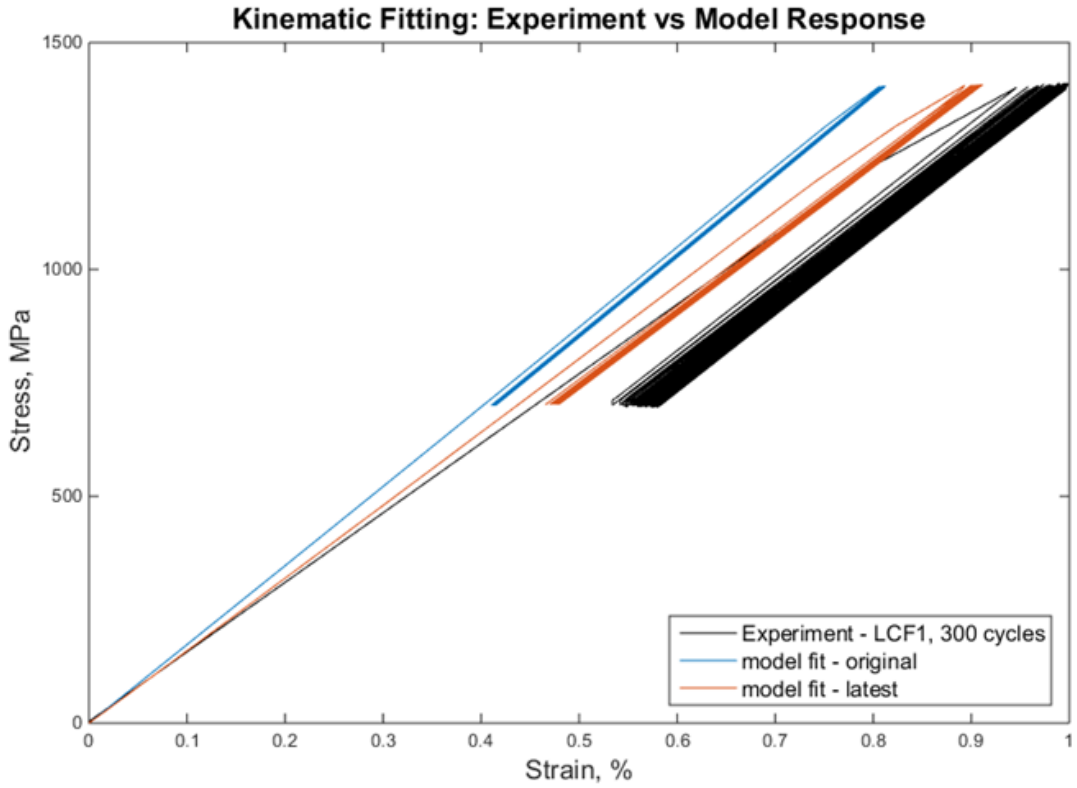

Figure 4.16: Comparisons of the initial and intermediate parameter calibrations to the LCF1 strain ratcheting experiment.

Table 4.7: Values of the constitutive parameters for the revised model calibration (UMAT v110e)

C_{11}	C_{12}	C_{44}	$\dot{\gamma}_o$	n	D_o	τ_o	ρ_o
237,321 (MPa)	118,120 (MPa)	92,756 (MPa)	7.2×10^{16} (s^{-1})	18	195 (MPa)	75.15 (MPa)	3.0×10^9 (mm^{-2})
α_t	μ	b	n_k	c_{gr}		d_{gr}	f_{tw}
0.1	92,756 (MPa)	0.407 (nm)	1	9.432 ($MPa\sqrt{mm}$)		0.002 (mm)	0.1
C_χ	η_o	t	h_o	k_1	k_2	k_3	
2	68.0	0.0001 (mm)	1	100,000 (mm^{-1})	1.0	0.1	

correct for the inherent reduction in elastic stiffness from reduced volume fraction of

$\langle 111 \rangle$ texture. The sensitivity of the effective elastic modulus to changes in crystallographic texture can be seen from Fig 4.17 which plots the results of the rate jump test run on a 1000 grain SVE for pure $\langle 111 \rangle$, pure $\langle 001 \rangle$ and mixed texture using the intermediate fit of the elastic constants found in Table 4.6.

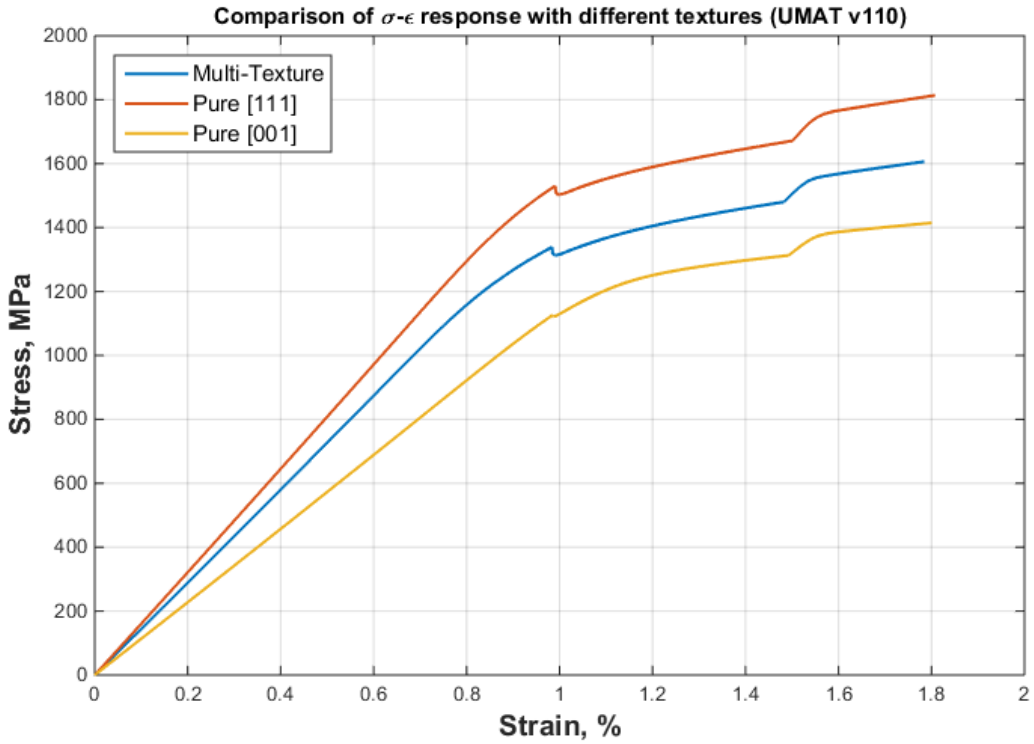

Figure 4.17: Sensitivity of the effective elastic modulus to SVE texture.

The material stiffness is highest for a pure $\langle 111 \rangle$ crystallographic texture, and reduces as the volume fraction of $\langle 111 \rangle$ is reduced to zero.

CHAPTER V

RESULTS AND DISCUSSION

5.1 FIP-Life Correlations

Several studies were undertaken using the newly developed CPFEM model in order to assess its efficacy for generating fatigue-life correlations in MP35N fine wires. The model results were compared to MP35N fatigue data available in literature and are presented in this chapter.

5.1.1 Effect of Inclusion Proximity to Surface

A parametric study was conducted to investigate the ability of the model to predict the effect of NMI surface proximity on fatigue life. The aim of the study was to replicate the inclusion surface proximity versus fatigue life trend of Full-Ti MP35N wire as demonstrated experimentally by the solid trend line in Figure 2.9. A Virtual Design of Experiments (VDoE) was created with four levels L_i corresponding to different NMI distances from the wire surface. Twenty microstructure instantiations were run at each level, in order to estimate the median fatigue life and scatter.

Each microstructure instantiation is a 20 μm^3 SVE occupying a volume immediately adjacent to the outer surface of the MP35N wire. The positive X-face is along the wire outer surface, and all other SVE faces are interior. Periodic boundary conditions are prescribed for the Y and Z faces and all edges. The positive X-face is traction-free and unconstrained, while the negative X-face is given a node-wise displacement boundary condition to mimic a periodic boundary. The negative X-face displacement boundary conditions are extracted from a reference analysis having fully 3D boundary conditions but identical mesh and loading history.

Each SVE was instantiated with 1000 grains according to the ellipsoid packing

method described in Sec 4.1.2. The grains were given a fiber texture with a single texture component normally distributed about the {111} orientation with standard deviation defined such that $2\sigma = 15°$. The full set of constitutive parameter values used in the study are given in Table 4.4.

The NMI distance from the wire surface x_{surf} was defined as the perpendicular distance from the wire surface to the nearest point of the NMI. Similarly, the centroid distance x_c was defined as the perpendicular distance from the wire surface to the NMI centroid. These and other geometry parameters for the NMI are illustrated in Figure 5.1. NMI size was fixed at 4 μm for all VDoE levels. The NMIs were oriented such that the inclusion faces were parallel to the SVE faces. All NMIs had their upper halves debonded from the matrix, as described in Sec 3.3.2. Values of the parameters relating to the NMI position at each level of the VDoE are given in Table 5.1.

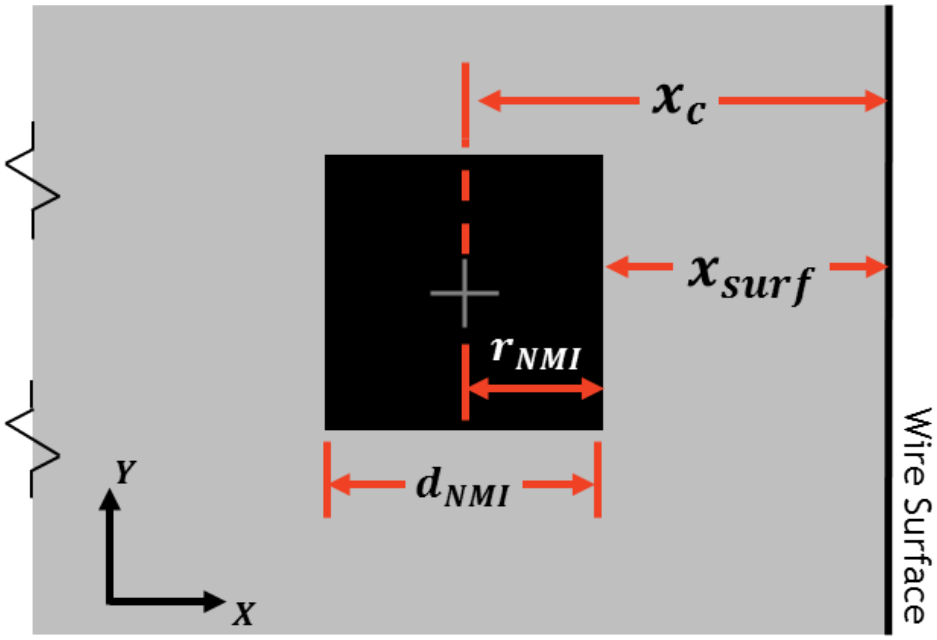

Figure 5.1: Subset of an SVE showing definitions of TiN particle geometry as related to the wire surface.

The loading profile applied to each microstructure instantiation was in the form of three fully-reversed $R = -1$ displacement controlled cycles. Figure 5.2 shows the form of the loading profile applied to the SVEs. This history is intended to replicate

Table 5.1: Values of NMI geometry parameters at each level of the virtual DoE

L_i	1	2	3	4
$\mathbf{x_{surf}}$	0.75 μm	1.5 μm	2.0 μm	4.0 μm
$\mathbf{x_c}$	2.75 μm	3.5 μm	4.0 μm	6.0 μm
$\mathbf{r_{NMI}}$	– 2.0 μm –			
$\mathbf{d_{NMI}}$	– 4.0 μm –			

loads experienced under RBBF by a small surface volume. Loading was applied along the global Y-axis, parallel to the wire neutral axis at the bend apex. The assumption that spin-fatigue fractures occur predominantly near the bend apex where loads are fully reversed and orthogonal to the neutral axis is supported by Schaffer [19] and is maintained in this study.

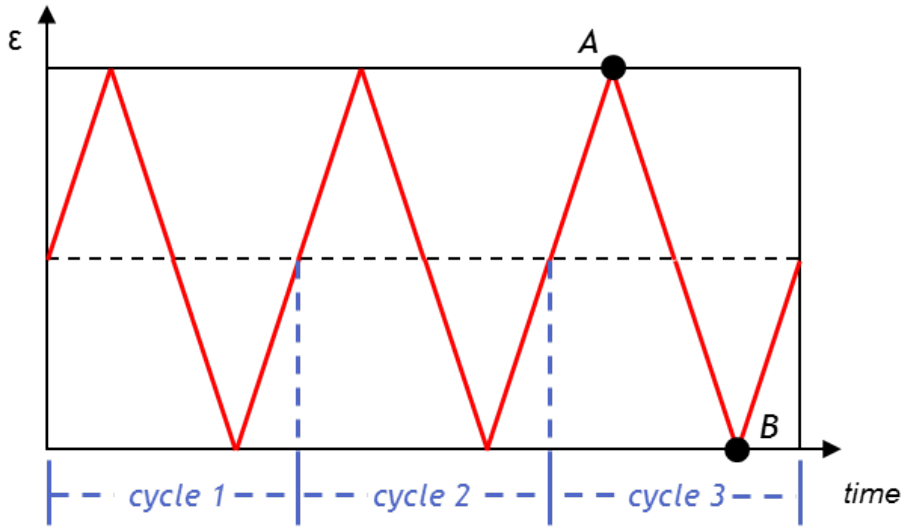

Figure 5.2: Loading profile applied to each SVE to simulate RBBF. Points A and B are the step endpoints used in the FS FIP calculations.

The magnitude of the loading amplitude at level L_i calculated based on the far-field stress S_{YY} at the NMI centroid. Since the main difference between each VDoE level is the NMI proximity to the wire surface, the load amplitude will be different for

each level. The far-field stress parallel to neutral axis of a wire in rotating bending is a strong function of the depth x beneath the wire surface. At the outer fiber, S_{YY} is a maximum, equal to the stress amplitude S_a in Eq. 2.3. At the neutral axis S_{YY} is zero. In general, neglecting microstructural inhomogeneity, the far-field stress S_{YY} is a linear function of depth x beneath the wire surface, expressed as

$$S_{YY}(x) = -\frac{S_a}{r_{wire}}(x) + S_a \tag{5.1}$$

where r_{wire} is the radius of the wire undergoing RBBF, and the quantity $-\frac{S_a}{r_{wire}}$ is the far-field stress gradient along the x-axis. In the ideal case, the SVE would be loaded with a linearly varying load along X as described by Eq. 5.1. However, non-uniform loads are incompatible with periodic boundary conditions due to the need to drive displacement boundary conditions from a single reference node. In order to maintain periodic boundary conditions while matching the stress state in the region of interest as closely as possible, the displacement on the reference node was determined by conversion from the far-field stress at the NMI centroid. This value was computed by inputting the appropriate value of x_c for each level L_i of the VDoE, such that

$$S_{YY}^{L_i} = -\frac{S_a}{r_{wire}}(x_c^{L_i}) + S_a \tag{5.2}$$

The far-field stress value determined for each level was converted into a strain amplitude and then to displacement amplitude by

$$\varepsilon_a = \frac{S_{YY}^{L_i}}{E} \tag{5.3}$$

and

$$Y_a = 20\ \mu m \cdot \varepsilon_a \tag{5.4}$$

with E being the elastic modulus of the MP35N wire and 20 μm being the length dimension of an SVE along the loading axis. This step was taken to closely match

of the far-field stresses in the FS AVs positioned along the NMI debond perimeter to the actual localized stresses generated by the RBBF experiments. Table 5.2 presents the relationships between the beam-bending stress amplitude at the wire apex, NMI surface proximity and SVE applied stress and strain amplitudes for the VDoE.

Table 5.2: Relationships between beam-bending stress reported at the wire apex (S_a) and stress (S_{YY}) and strain (ε_a) amplitudes applied to the SVE

$\boldsymbol{L_i}$	$\boldsymbol{x_{surf}}$ ($\boldsymbol{\mu m}$)	$\boldsymbol{S_a}$ (MPa)	$\boldsymbol{S_{YY}}$ (MPa)	$\boldsymbol{\varepsilon_a}$ (% of $\boldsymbol{\varepsilon_y}$)
1	0.75	620	586	0.331
2	1.5	620	577	0.325
3	2.0	620	570	0.322
4	4.0	620	546	0.308

The fidelity near the NMI comes at the expense of accuracy far from the NMI centroid along the X axis, but this is considered acceptable since the material response in these regions does not enter into the FS calculations. Figure 5.3 shows how the SVE stress amplitude used in the study compares to the S_{YY} stress gradient between the outer surface and the neutral axis.

Twenty microstructure instantiations were run at each of the four NMI depths 0.75, 1.5, 2.0 and 4.0 μm. The maximum volume-averaged FS parameter was computed for each run as described in Sec 3.3.1 and Sec 3.3.2. Figure 5.4 shows the EV FS values plotted against NMI distance from surface.

The EV FS values plotted in Figure 5.4 were correlated to fatigue life values through the Modified Tanaka-Mura approach from Sec 3.5. The correlation to life was performed at the 0.75 μm level assuming negligible propagation life. The median EV FS value was correlated to the linear regression fit the experimental data points with $d_{gr} = 1.5$ μm. A correlation coefficient $\alpha = 1.129 \times 10^{-5}$ μm–cycles was found to

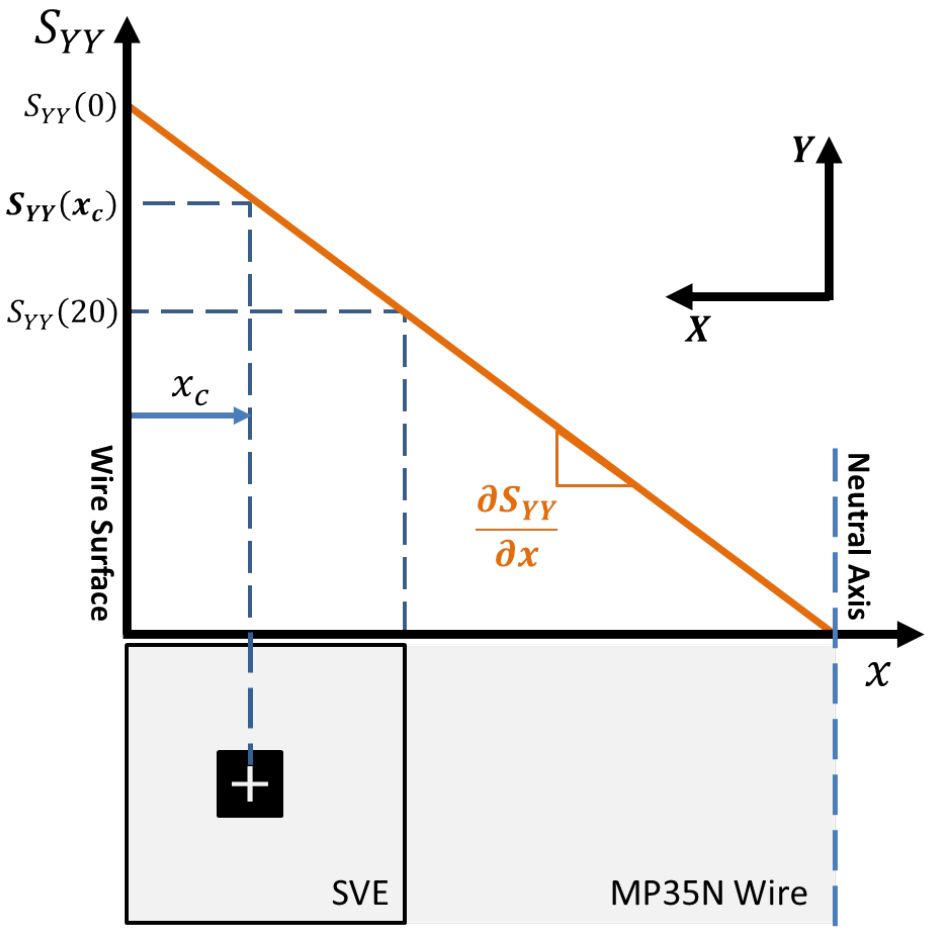

Figure 5.3: Selection of stress amplitude for an SVE. Stress amplitude S_{YY} decreases linearly with NMI depth x_c due to the stress gradient generated in bending. Note that the x axis for depth is opposite the global X axis.

correlate well to experiment. The three remaining VDoE levels were correlated using the same values of α and d_{gr}. The resulting life-correlations are plotted against the experimental data points in Figure 5.5.

As expected, the life-correlation results show increasing life values as the NMI depth from the free surface is increased. Moreover, the model results show good overlap with the linear regression trend computed from the experimental data points at all depths considered in the VDoE. The minimum lives predicted by the model at each level is below the 5% confidence bound. This indicates that the model gives a more conservative prediction of minimum fatigue life than the regression fit. The accuracy

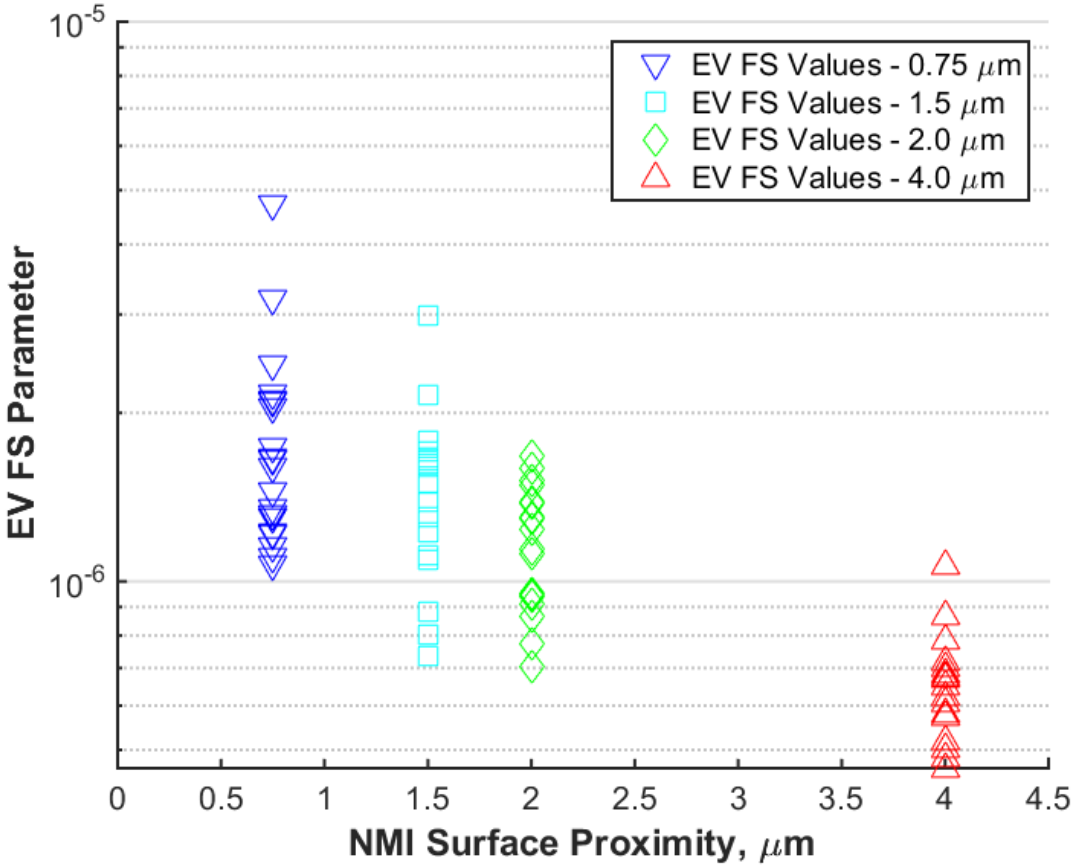

Figure 5.4: Extreme-value FS parameter values for four distinct NMI depths and corresponding stress amplitudes

of the trendlines derived from experiment could be improved if more experimental fatigue data points were obtained having a failure initiating from a near-surface TiN inclusion. Similarly, confidence in the minimum life value predicted by the model at each NMI depth could be improved by running additional microstructure instantiations at that condition.

The distribution of lives at each NMI depth can be further investigated by examining the empirical CDFs and fitting GEV distributions. The GEV distributions are fitted to the data using Statistics Toolbox feature of MATLAB. The empirical CDFs along with the fitted GEV distributions are plotted in Figure 5.6.

Plotting the CDFs allows for comparison of the probability of failure at a given

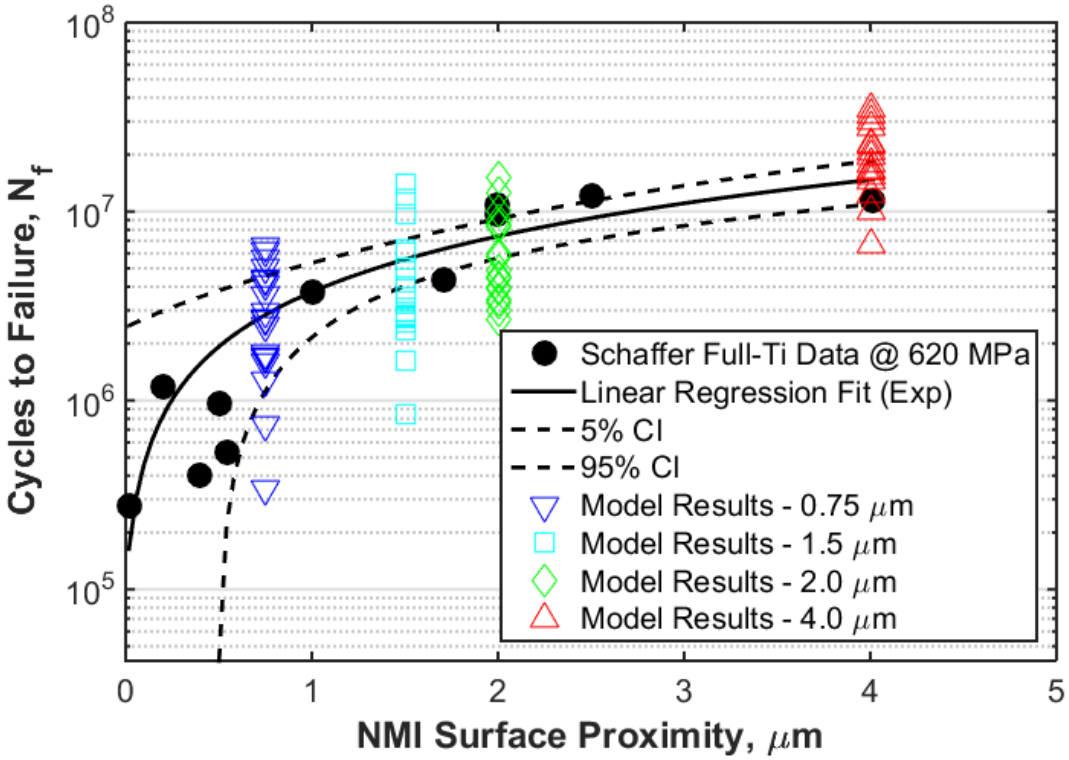

Figure 5.5: Life correlations of the model fit to experimental data. The modified T-M fit is performed at the 0.75 μm level resulting in a correlation coefficient α of 1.129×10^{-5} μm-cycles.

number of cycles N_f among differing NMI depths from the wire surface. Based on the figure, the probability of failure at 1×10^7 cycles is predicted to be 1 for $x_{surf} = 0.75$ μm, 0.94 for $x_{surf} = 1.5$ μm, 0.85 for $x_{surf} = 2.0$ μm but only 0.07 for $x_{surf} = 4.0$ μm. This result demonstrates that the probability of failure drops off drastically once x_{surf} reaches or exceeds d_{NMI}. This is consistent with past studies [18], which have found that fully embedded NMIs with $x_{surf} \geq d_{NMI}$ are associated with substantially lower fatigue potencies than those close to the surface. The reduction of fatigue potency with increasing depth is enhanced by the stress gradient in RBBF fatigue. These stress gradients are not present in fatigue specimens in tension-compression or tension-tension fatigue. The fitting parameters for the GEV distributions are given in Table 5.3.

Gumbel CDFs were also fit to the data and the fit was compared to the GEV

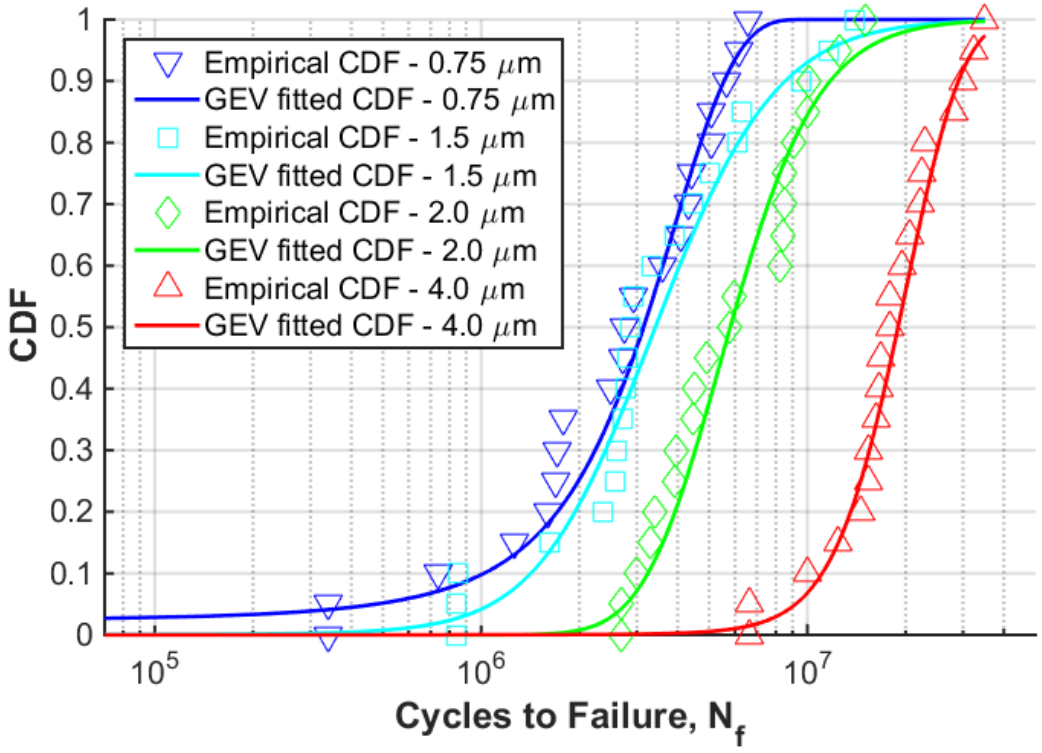

Figure 5.6: CDFs of the Fatigue-life correlations with corresponding GEV distributions.

Table 5.3: Fitting Parameters for GEV CDFs

x_{surf} (μm)	μ	σ	ξ	Type
0.75	2.554×10^6	1.679×10^6	-0.214	III (Weibull)
1.5	2.727×10^6	1.780×10^6	0.314	II (Fréchet)
2.0	4.937×10^6	2.250×10^6	0.250	II (Fréchet)
4.0	1.668×10^7	6.336×10^6	-0.131	III (Weibull)

case. The fit is shown in Figure 5.7. By comparing to Figure 5.6, it can be seen that the GEV CDFs give a better fit, especially at probabilities of failure from 0 to 0.2. The Gumbel distribution fit is especially poor for $x_{surf} = 1.5\mu m$.

The Gumbel distributions predict no minimum life value for the values of x_{surf} investigated because the CDFs approach zero probability of failure slowly as N_f goes to zero. Table 5.4 lists the fitting parameters for the Gumbel distributions. The

restriction of ξ to 0 results in the poor fits to the empirical CDFs at the low likelyhood end of the distributions.

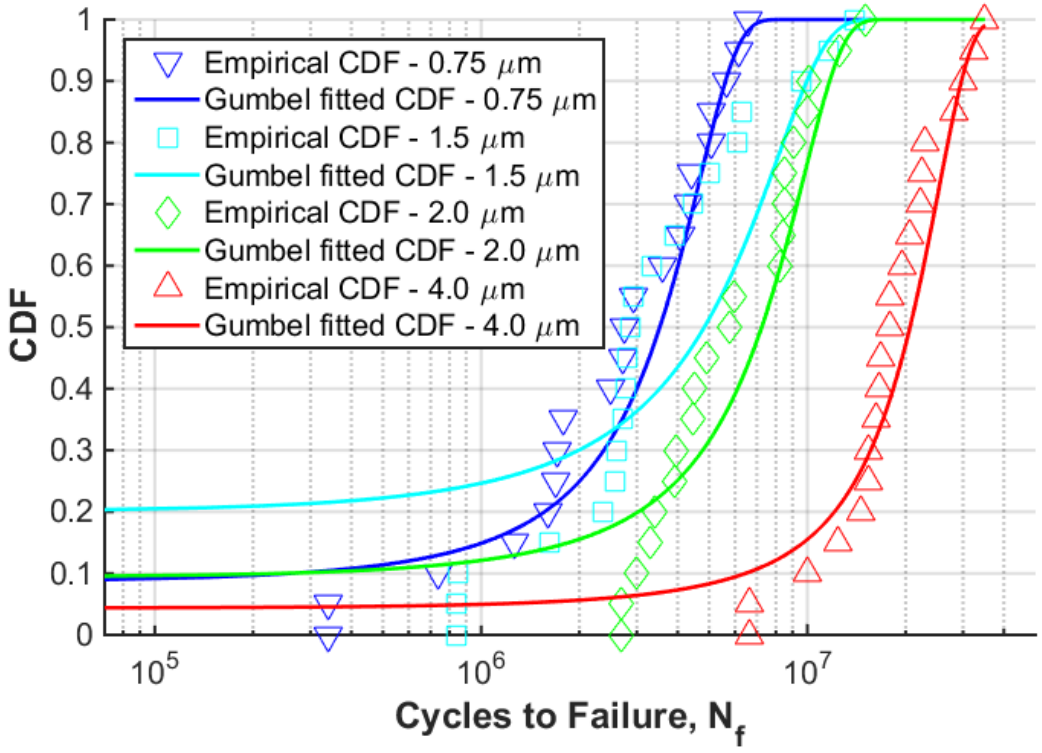

Figure 5.7: CDFs of the fatigue-life correlations with fitted Gumbel distributions.

Table 5.4: Fitting Parameters for Gumbel CDFs

x_{surf} (μm)	μ	σ	ξ
0.75	4.163×10^6	1.733×10^6	0
1.5	6.394×10^6	4.273×10^6	0
2.0	8.600×10^6	3.712×10^6	0
4.0	2.337×10^7	7.511×10^6	0

5.1.2 Identifying the Crack Incubation to Microcrack Growth Transition

A second study was conducted to identify the transition life between fatigue crack incubation and microcrack growth regimes using Eq. 3.12 to correlate to an additional

MP35N fatigue-life dataset. The transition life value N_t can be considered as the value of N_f where dominant fatigue mechanism switches from large-scale plasticity and microcrack growth to crack incubation due to highly localized damage accumulation [24]. Previously, this quantity was estimated by equating the stress-life and strain-life equations and solving for N_t, but the use of a constitutive fatigue model offers an alternative basis for its estimation which explicitly considers the underlying fatigue mechanisms. Because the FS parameter as employed in this model directly equates the accumulation of localized cyclic shear strain with crack incubation potency most associated with incubation, the transition life N_t may be identified as the point of divergence between the experimental S-N curve and the model T-M correlation to the incubation regime. At stress amplitudes above this transition, fatigue life is dominated by the cycles to propagate the crack through the wire, with the result that the model produces overly conservative life estimates based on incubation life.

The experimental fatigue-life data used in this study was obtained from Prasad et al [14]. They conducted RBBF on 100 μm diameter as-drawn low-Ti MP35N wire at seven stress amplitudes ranging from 1650 MPa (the 0.2% offset yield strength) down to 550 MPa. They also performed tension-tension fatigue (TTF) with a stress ratio R = 0.3 on the same wire. An S-N diagram of the fatigue data is presented in Fig 5.8. Here, squares represent the RBBF data and circles represent TTF. Filled shapes indicate fractures and open shapes indicate runouts. The runout criteria for these experiments was 1×10^7 cycles. Note that RBBF tests are displacement controlled, with displacement amplitude being converted to stress amplitude for comparative purposes, as described in Sec 2.2. The displacement controlled nature of RBBF means that the stress intensity factor range, defined as $\Delta K = K_{\max} - K_{\min}$ and linked to the rate of crack growth per cycle $\frac{da}{dN}$ via the Paris law relation, likely decreases as the crack grows due to the increased compliance of the wire with larger crack size. In contrast, TTF are force-controlled tests, with ΔK generally increasing with crack

growth. Because the increased rate of crack growth as well as the positive mean stress, it is expected that the life to failure in TTF is controlled by crack formation at all stress amplitudes and does not exhibit a crack growth dominated regime.

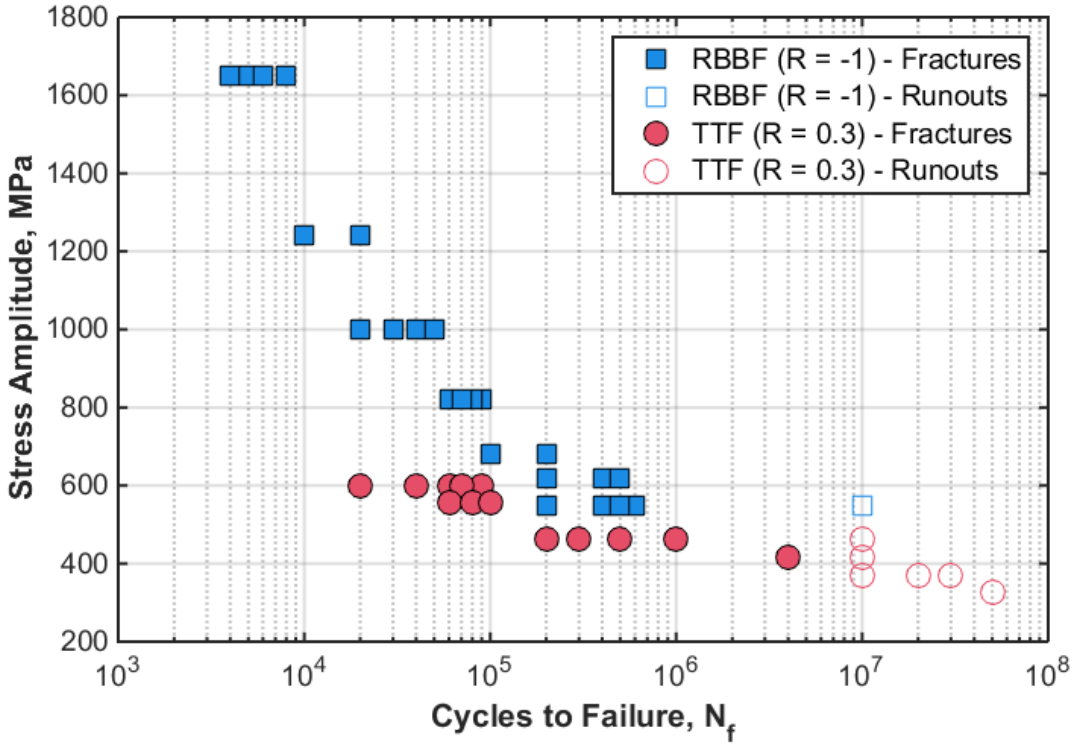

Figure 5.8: Prasad et al. S-N data for as-drawn low-Ti MP35N wire [14].

Comparing the RBBF and TTF fatigue data in Fig 5.8, it is seen that the TTF life distribution is below that of the RBBF at every comparable stress amplitude. One contributing factor is the difference in the highly stressed volume due to the test geometry. For equivalent $S_{\max}$, assuming uniform spatial defect distributions, the likelihood of finding a fatigue hotspot with sufficient driving force to nucleate a fatigue crack increases in proportion to the size of the highly stressed volume. A larger highly stressed volume samples a much larger subset of the defect population within an individual test specimen and biases the fracture initiation toward higher potency flaws leading to earlier crack nucleation and reduced fatige life. In addition, the likelihood of multiple cracks forming independently and later coalescing into a single

large crack increases when the highly stressed volume occupies a significant portion of the overall specimen. In TTF, the full wire cross section along the entire 255 mm gage length between the grips is subject to the maximum stress $S_{\max}$. In contrast, only a small portion of the wire near the wire surface and the bend apex approaches $S_{\max}$ in RBBF tests. The difference in highly stressed volume can be estimated by computing the ratio $V_{\text{TTF}} : V_{\text{RBBF}}$. For a 100 μm diameter wire, $V_{\text{TTF}} = \pi\,(r_o)^2\,\ell_{\text{gage}} = \pi \cdot (0.05\text{ mm})^2 \cdot (255\text{ mm}) \approx 2.0\text{ mm}^3$. An approximation for V_{RBBF} can likewise be made considering an annulular cross-section 5 μm from the outer wire radius over a length extending 5 mm on either side of the bend apex. The latter assumption is supported by Schaffer's finding that 90% of RBBF fractures occur less than 5 mm from the bend apex [19]. Based on these assumptions V_{RBBF} is then calculated as $V_{\text{RBBF}} = \pi\big[(r_o)^2 - (r_i)^2\big]\,\ell_{\text{apex}} = \pi \cdot \big[(0.05\,\text{mm})^2 - (0.045\,\text{mm})^2\big] \cdot (10\,\text{mm}) \approx 0.015\,\text{mm}^3$. This provides an estimate of the highly stressed volume ratio with V_{TTF} being 133 times greater than V_{RBBF}.

Microstructures for the model correlation were instantiated as described in Sec 5.1.1 except that all NMIs were centered in the SVE and fully 3D periodic boundary conditions were prescribed. Ten microstructure instantiations were generated at each of five stress amplitudes 1000, 820, 680, 620 and 550 MPa, corresponding to the five lowest stress amplitudes in the Prasad data. No stress adjustments for the NMI depth from the wire surface as in Eq. 5.1 were undertaken, instead the far-field stress at the NMI was set equal to the fully-reversed stress amplitude at the wire surface. In other words, each SVE was instantiated with a 4 μm cuboidal inclusion with a applied load commensurate with that at the wire surface, but neglecting the traction-free boundary which was modeled in the prior study. In testing it was found that the impact of boundary effects on local FIP response was overwhelmed by the much larger effect of changing the alternating stress amplitude. The constitutive model parameters for this study are given in Table 4.7 and were selected to reflect a wire

with significant texture components in the ⟨001⟩, ⟨111⟩ and ⟨113⟩ directions with respect to the wire neutral axis.

The EV FS responses for two separate values of the FS stress weighing coefficient, k^* are plotted in Fig 5.9 at the five RBBF stress amplitudes in order to assess the model sensitivity to k^* (datasets have been offset in the y-axis for clarity). The EV FS parameter values are largely unchanged between the two datasets. Based on this comparison, it is seen that the FS parameter has a low sensitivity to the choice of k^* for all stress amplitudes evaluated. Therefore, the following T-M life correlations will use $k^* = 1$ for consistency with those in Sec 5.1.1.

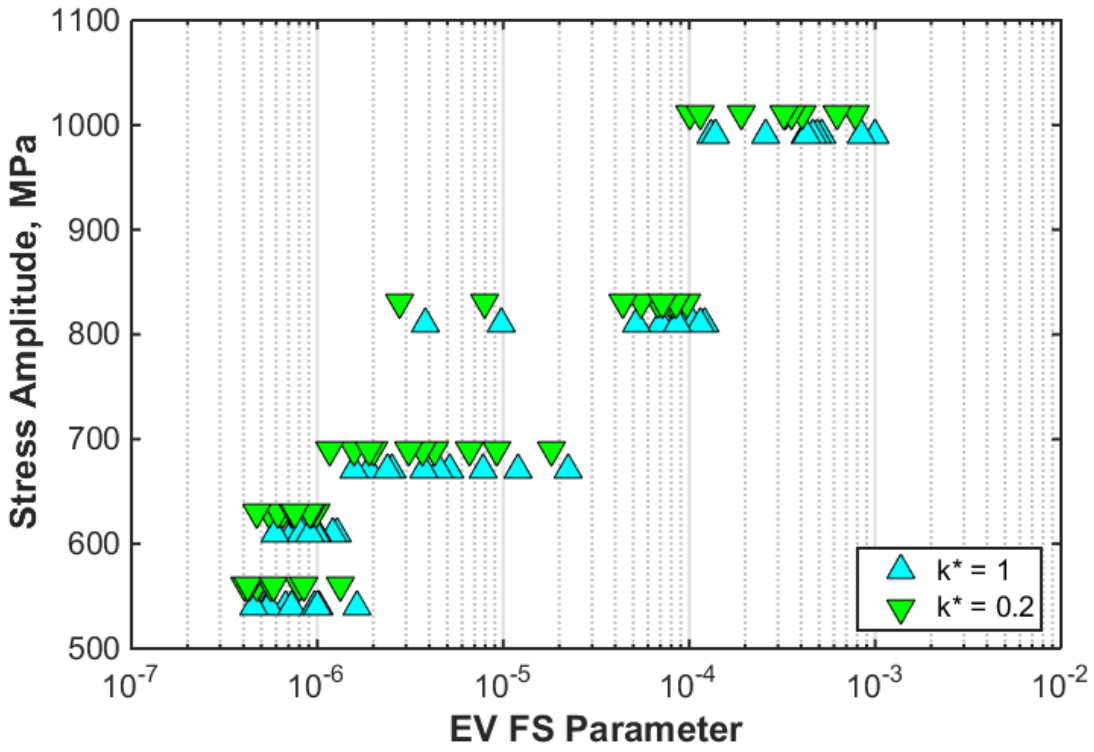

Figure 5.9: Comparison of Extreme-Value FS parameter responses using weighting coefficients $k^* = 1$ and $k^* = 0.2$.

The T-M correlation of the model EV FS response to the Prasad RBBF data was undertaken at the 620 MPa stress amplitude because it was the lowest stress amplitude without runouts which generally are found to be dominated by crack formation. Using

$d_{gr} = 2$ μm, the correlation coefficient α was found to be $4.995 \times 10^{-7}\mu$m-cycles. Figure 5.10 shows the resultant fit with the model results plotted as crosses. The model correlation shows good agreement with experimental data at 550 MPa but begins to diverge at the 680 MPa stress amplitude. Above 680 MPa, the model results are overly conservative compared the experimental data, suggesting that the life is dominated by propagation life. This indicates that the transition from crack formation to propagation for the RBBF data is within the range of life values in the 680 MPa stress amplitude. It is also noted that the slope of the model correlation is close to that of the TTF data, indicating that the model would likely produce a good fit to the TTF data for all stress amplitudes represented.

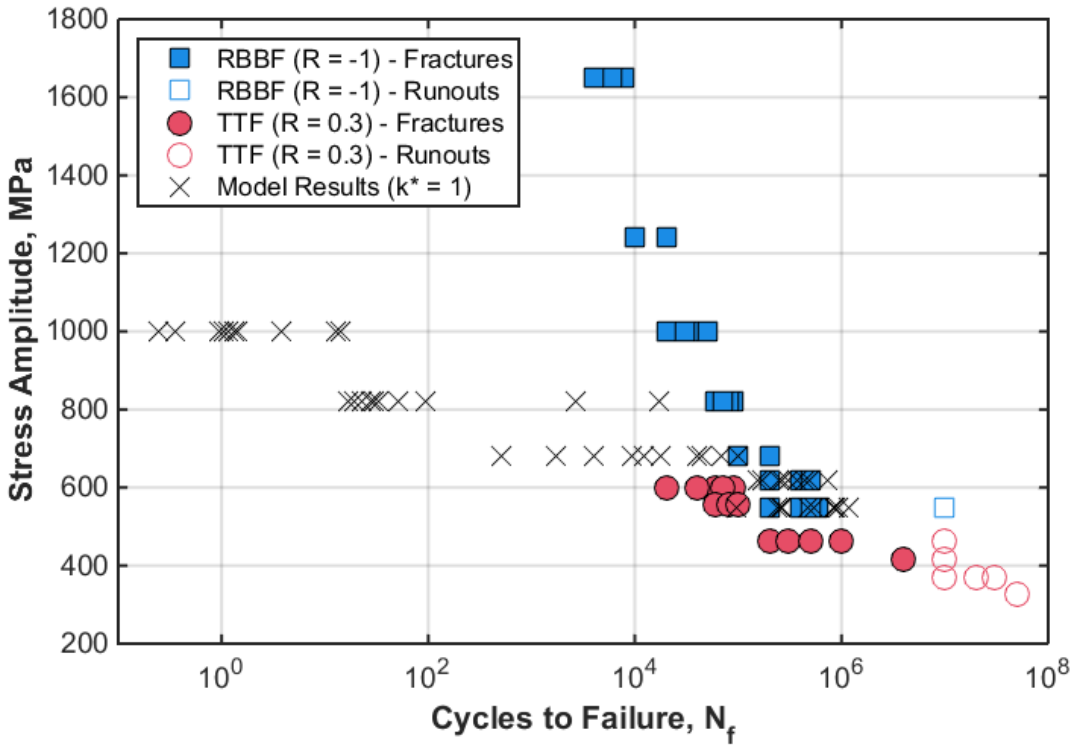

Figure 5.10: Fatigue-life correlation to Prasad et al. RBBF data at 620 MPa with T-M correlation coefficient $\alpha = 4.995 \times 10^{-7}$ μm-cycles.

The overlap between the model correlation and the RBBF data is examined close to the 680 MPa stress amplitude in order to estimate the value of N_t predicted by

the model. Figure 5.11 shows a close-in view of the point of divergence between the model and experimental data sets in Fig 5.10. From this figure, it can be seen that the value of N_t is very close to 1×10^5 cycles. At life values below 1×10^5 cycles, the model T-M correlation underpredicts the RBBF data indicating that microcrack growth dominates the total life to failure. At life values above 1×10^5 the model correlates well to the RBBF data, indicating that HCF mechanisms captured by the model - namely crack formation due to localized cyclic slip accumulation - are the main contributors to fatigue fracture. The RBBF fractures at the 680 MPa stress amplitude represent the transitional stress where crack formation and microcrack growth contribute to the total life in roughly equal measure.

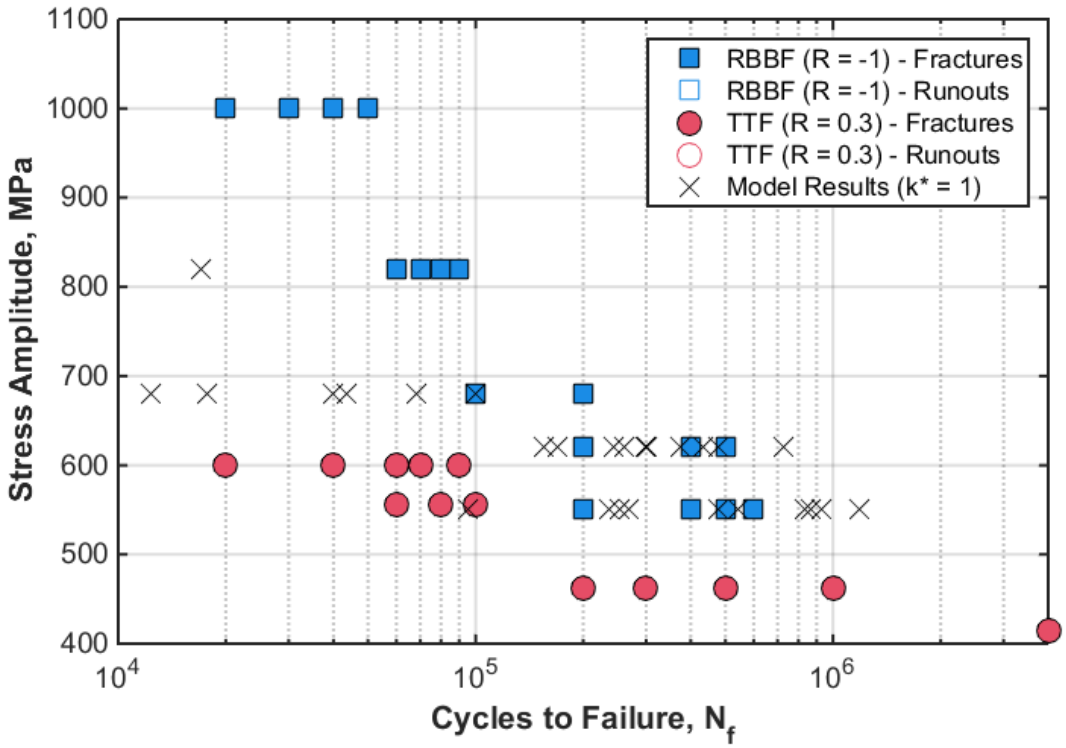

Figure 5.11: Close-in view of the point of divergence between the T-M correlation to the RBBF data at 680 MPa and 1×10^5 cycles.

Another indication that the transitional stress amplitude occurs at 680 MPa is provided by the increased scatter of the model data compared to the other stress

levels. This can be seen intuitively by looking at either the life correlations in Fig 5.10 or the EV FS responses in Fig 5.9, but the EV FS response provides more direct insight into the model behavior. To quantify the variability at a given stress amplitude, a weighted EV FS variability parameter Ω_{FS} is defined as

$$\Omega_{FS}(S_a, m) = \frac{\Delta P_{FS}(S_a, m)}{\tilde{P}_{FS}(S_a, m)} \tag{5.5}$$

with S_a being the stress amplitude considered and m being the number of instantiations run at that amplitude. The quantity ΔP_{FS} is the range of EV FS parameter defined as $\Delta P_{FS} = \max(P_{FS}) - \min(P_{FS})$ and $\tilde{P}_{FS}$ is the median of the EV FS values. Weighting the observed scatter by $\tilde{P}_{FS}$ allows for a comparison to be made between FS response parameters spanning several orders of magnitude. Figure 5.12 shows a bar graph of Ω_{FS} using the $k^* = 1$ FS response values for the five stress amplitudes modeled with 10 microstructure instantiations each. From this plot, it is seen that the weighted variability at 680 MPa is 5.03, which is more than twice as large as the next largest value, 1.95, at 1000 MPa. Moreover, the value of Ω_{FS} at 680 MPa is more than three times larger than the values at its neighboring stress amplitudes. The spike in Ω_{FS} at 680 MPa suggests a heightened sensitivity of the EV FS response to the microstructural features along the NMI debond interface, which can be associated with a switch in the dominant fatigue mechanism.

The value of Ω_{FS} is sensitive to the number of microstructure instantiations run. Since only a small number of microstructure instantiations were run, the values obtained should be treated as a comparative metric only and not representative of the true fatigue variability. Adding additional microstructure instantiations will improve the Ω_{FS} estimates until the point when EV FS distribution becomes converged.

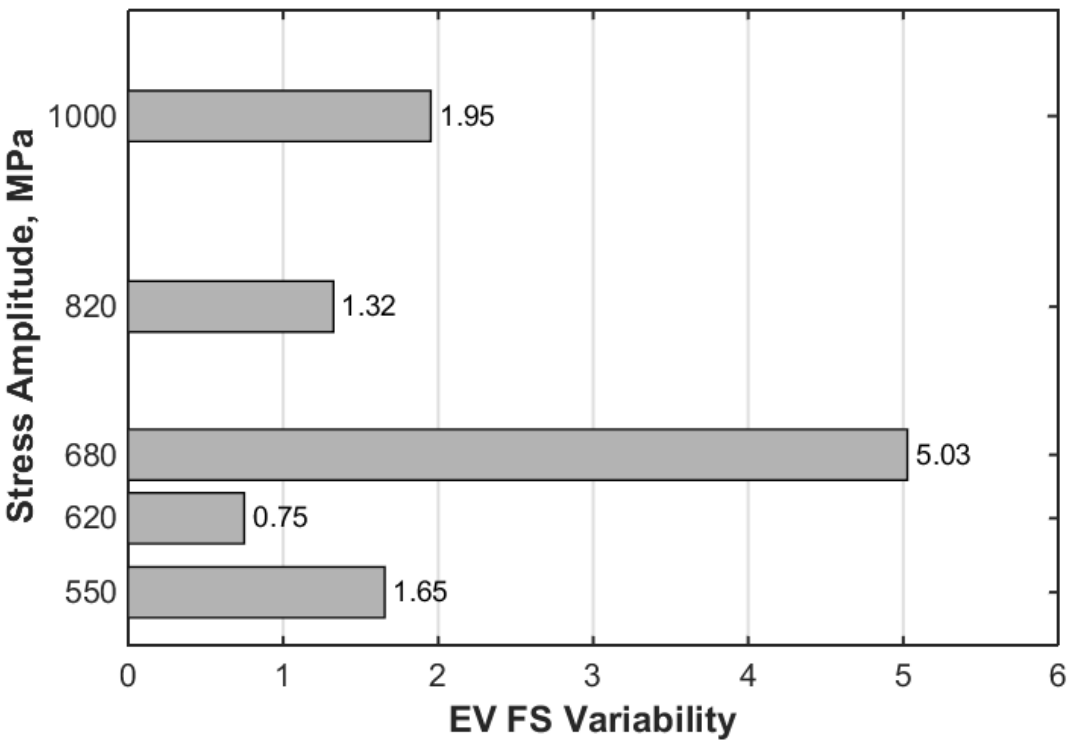

Figure 5.12: Weighted variability (Ω_{FS}) in EV FS response parameters at the five stress amplitudes modeled with 10 microstructure instantiations each.

CHAPTER VI

CONCLUSIONS

A physically-based, rate-dependent crystal viscoplasticity constitutive model was developed building off the work of Shenoy [21] which represents the isothermal mechanical behavior of single-phase fcc MP35N alloy material. Deformation processes at and above the grain scale are modeled, including accumulation of plastic shear strain on preferred slip systems and isotropic and kinematic hardening. The model also accounts for hardening due to nano-scale twinning through a homogenization approach. The model parameters were fit to experimental monotonic tensile loading curves and cyclic tension-tension experiments promoting strain ratcheting and adequately model the material behavior under monotonic and cyclic loading conditions.

A microstructure generation tool was developed to construct statistical volume elements (SVEs) reflecting the fine-grained microstructure and fiber texture characteristic of MP35N fine wire. This includes (1) an algorithm for seeding ellipsoidal grains by sampling from a lognormal distribution matched to experimentally characterized grain size distributions for MP35N wire, (2) the ability to impose non-random grain texture distributions mimicking MP35N EBSD scans with fiber texture, (3) a scheme for placing hard non-metallic inclusions (NMIs) into SVEs with control over the NMI-matrix interface, and (4) a meshing algorithm to maximize resolution of stress gradients near the NMI while maintaining computational efficiency to run fatigue loading cycles within the ABAQUS finite-element solver.

A modified Tanaka-Mura incubation life correlation methodology was employed to

correlate the volume-averaged extreme-value Fatemi-Socie parameter near the NMI-matrix interface with the HCF behavior of MP35N wire. The model correctly predicted the fatigue life behavior resulting from variation of NMI proximity to the wire surface in full-Ti MP35N wires run under rotating beam bending fatigue (RBBF) loading at 620 MPa. A significant reduction in fatigue potency was found when NMIs became fully embedded ($x_{surf} \geq d_{NMI}$) in the wire, consistent with experimental results. The same correlation scheme was also used to identify the transition life N_t between crack incubation and microcrack growth dominated fatigue regimes for low-Ti MP35N wire loaded in RBBF. The transition life was estimated to be $N_t = 1 \times 10^5$ cycles based on the point of divergence between the model correlation at 680 MPa and the S-N curve. At life values above N_t, the model fit showed good overlap with the experimental data, but a life values below N_t the model fit was overly conservative for RBBF, indicating that crack formation was no longer the dominant fatigue mechanism. It is anticipated that the model would correlate well to the TTF dataset due to the reduced amount of microcrack growth present in force-controlled modes of fatigue.

CHAPTER VII

RECOMMENDATIONS FOR FURTHER STUDY

The results presented in this work are by no means an exhaustive exploration of all applications and uses for the model. A number of recommendations for continued study are put forth here which go beyond the scope of the current work.

7.1 Ranking of Microstructure Attributes by Fatigue Potency

A ranking scheme to categorize and rank the microstructure attributes by fatigue potency could be employed to identify the microstructure configurations with the highest impact on fatigue life. The impact of NMI proximity to the free surface has already been considered in Ch. 5. Additional microstructure attributes which may be of interest include the morphology, size and composition of the NMI, the configuration of the NMI-matrix interface, and the presence of other defect types such as surface scratches or sub-surface voids. These attributes can be compared and ranked through the use of extreme-value marked correlation functions as employed by Przybyla [16]. The use of these functions allows different microstructure attributes to be ranked by their impact on fatigue and can also assess the impact of interactions between microstructure attributes.

7.1.1 NMI Morphology

It is of interest to study the impact of inclusion morphology on fatigue crack initiation potency. In addition to the cuboidal shapes considered in this work, spherical, elliptical and octahedral inclusion geometries may also be considered. In the cases of octahedral or cuboidal inclusions, the presence of sharp corners may add stress risers

in addition to those which are already present due to the strain mismatch between the matrix and the embedded NMI particle. In these cases, the orientation of the NMI with respect to the principle loading axis is an additional consideration that should not be neglected.

7.1.2 NMI-matrix Interface

The condition of the NMI-matrix interface should also be considered in assessing the microstructure for fatigue initiation potency. Interface delamination between the matrix and the NMI particle can cause a heightened stress state and serve as an embryonic crack from which the crack can propagate into the matrix. The extent of the NMI-matrix delamination along with its orientation in relation to cyclic loading axis dictates its potency to drive the generation and growth of fatigue cracks. Some common interface conditions observed include fully bonded, partially debonded, fully debonded and cracked NMIs.

While the present work has investigated partially debonded NMIs due to a preliminary assessment that this condition represented a high driver for crack initiation, the relative potency of these NMI-matrix interface conditions has not been rigorously established. The microstructure generation tool has options to select from several NMI-matrix interface scenarios on a cuboidal inclusion, and could be adapted to mesh others. Figure 4.2 shows some of the NMI-matrix debonding scenarios available in the microstructure generation tool.

7.1.3 Alternative Crack Initiation Sites

In the prior discussion, it has been assumed that fatigue cracks initiate at NMIs associated with the generation of local stress risers and elastic mismatch strains. However, other types of crack initiation sites are possible and are sometimes observed in fine MP35N wires. Other defects which have been observed in MP35N wires are surface scratches from the die drawing process and large grain-mediated crack initiation.

Surface scratches act in a similar manner to notches. Fatigue crack initiation due to notches was explored by Musinski [11]. The role of large-grain mediated crack formation in HCF can also be addressed using the current methodology, provided data on large-grain distributions in the drawn wire is available.

REFERENCES

[1] Asgari, S., El-Danaf, E., Shaji, E., R., K. S., and Doherty, R. D., "The secondary hardening phenomenon in strain-hardened MP35N alloy," *Acta Metallurgica*, vol. 46, no. 16, pp. 5795–5806, 1998.

[2] ASTM F562-13, "Standard specification for wrought 35cobalt-35nickel-20chromium-10molybdenum alloy for surgical implant applications (UNS R30035)," 2013.

[3] Castelluccio, G. M. and McDowell, D. L., "Assesment of small fatigue crack growth driving forces in single crystals with and without slip bands," *International Journal of Fracture*, vol. 176, pp. 49–64, 2012.

[4] Dassault Systemes, "Abaqus v6.14-1," 2014. Providence, RI, USA.

[5] El-Danaf, E., Kalidindi, S. R., and Doherty, R. D., "Influence of deformation path on the strain hardening behavior and microstructure evolution in low SFE FCC metals," *International Journal of Plasticity*, vol. 17, pp. 1245–1265, 2001.

[6] Fatemi, A. and Socie, D., "A critical plane approach to multiaxial fatigue damage including out-of-phase loading," *Fatigue and Fracture of Engineering Materials and Structures*, vol. 11, no. 3, pp. 149–165, 1988.

[7] Li, B. and Steigauf, T., "Crystallography texture and mechanical properties of MP35N wire," in *Materials Processes for Medical Devices Conference*, ASM, September 2007.

[8] MathWorks, Inc, "Matlab, R2014b," 2014. Natick, MA, USA.

[9] Musinski, W., *Modeling the Effects of Shot-Peened Residual Stresses and Inclusions on Microstructure-sensitive Fatigue of Ni-Base Superalloy Components*. PhD thesis, Georgia Institute of Technology, August 2014.

[10] Musinski, W. D., "Novel methods for microstructure-sensitive probabilistic fatigue notch factor," Master's thesis, Georgia Institute of Technology, August 2010.

[11] Musinski, W. D. and McDowell, D. L., "Microstructure-sensitive probabilistic modeling of HCF crack initiation and early crack growth in Ni-base superalloy IN100 notched components," *International Journal of Fatigue*, vol. 37, pp. 41–53, 2012.

[12] Office of Science and Technology Policy, "Materials genome initiative for global competitiveness," white paper, National Science and Technology Council, June 2011.

[13] Ornberg, A., Pan, J., Herstedt, M., and Leygraf, C., "Corrosion resistance, chemical passivation, and metal release of 35N LT and MP35N for biomedical material application," *Journal of the Electrochemical Society*, vol. 154, no. 9, pp. C546–C551, 2007.

[14] Prasad, M., Reiterer, M., and Kumar, K., "Microstructure and mechanical behavior of an as-drawn MP35N alloy wire," *Material Science & Engineering A*, vol. 610, pp. 326–337, 2014.

[15] Przybyla, C. P., *Microstructure-sensitive Extreme Value Probabilities of Fatigue in Advanced Engineering Alloys*. PhD thesis, Georgia Institute of Technology, 2010.

[16] Przybyla, C. P. and McDowell, D. L., "Simulated microstructure-sensitive extreme value probabilities for high cycle fatigue of duplex Ti-6Al-4V," *International Journal of Plasticity*, 2011.

[17] Raghavan, M., Berkowitz, B. J., and Kane, R. D., "A transmission electron microscopic investigation of phase transformations in MP35N," *Metallurgical and Materials Transactions A: Physical Metallurgy and Materials Science*, vol. 11A, pp. 203–207, 1980.

[18] Salajegheh, N. and McDowell, D. L., "Microstructure-sensitive weighted probability approach for modeling surface to bulk transition of high cycle fatigue failures dominated by primary inclusions," *International Journal of Fatigue*, vol. 59, pp. 188–199, 2014.

[19] Schaffer, J. E., "A hierarchical initiation mechanism approach to modeling fatigue life variability in 35Co-35Ni-20Cr-10Mo alloy medical grade fine wire," Master's thesis, Purdue University, 2007.

[20] Schaffer, J. E., "An examination of fatigue initiation mechanism in thin 35Co-35Ni-20Cr-10Mo medical grade wires," *ASTM International*, vol. 5, pp. 1–10, July 2008.

[21] Shenoy, M., Tjiptowidjojo, Y., and McDowell, D. M., "Microstructure-sensitive modeling of polycrystalline IN 100," *International Journal of Plasticity*, vol. 24, pp. 1694–1730, 2008.

[22] Shenoy, M., Zhang, J., and McDowell, D. L., "Estimating fatigue sensitivity to polycrystalline ni-base superalloy microstructures using a computational approach," *Fatigue and Fracture of Engineering Materials and Structures*, vol. 30, pp. 889–904, 2007.

[23] Sorensen, D., Li, B., Gerberich, W., and Mkyoyan, K., "Investigation of secondary hardening in Co-35Ni-20Cr-10Mo alloy using analytical scanning transmission microscopy," *Acta Materialia*, 2013.

[24] Suresh, S., *Fatigue of Materials*. Cambridge University Press, second ed., 1998.

[25] Tanaka, K. and Mura, T., "A dislocation model for fatigue crack initiation," *Journal of Applied Mechanics*, vol. 48, pp. 97–103, 1981.

[26] Wang, Y., Wang, J. J., Zhang, H., Manga, V. R., Shang, S. L., Chen, L.-Q., and Liu, Z.-K., "A first-principles approach to finite temperature elastic constants," *Journal of Physics: Condensed Matter*, vol. 22, pp. 225404–225412, 2010.